
Article:
Bai, M., Namus, R., Xu, Y. et al. (3 more authors) (2019) In-situ Ti-6Al-4V/TiC composites synthesized by reactive spark plasma sintering : processing, microstructure, and dry sliding wear behaviour. Wear, 432-433. ISSN 0043-1648

https://doi.org/10.1016/j.wear.2019.202944

Manuscript Details

Manuscript number	WEA_2019_234_R2
Title	In-situ Ti-6Al-4V/TiC Composites Synthesized by Reactive Spark Plasma Sintering: Processing, Microstructure, and Dry Sliding Wear Behaviour
Article type	Full length article

Abstract

Titanium carbide (TiC) reinforced Titanium Matrix Composites (TMCs) have been synthesized via an in-situ reactive spark plasma sintering (SPS) process using commercial Ti-6Al-4V spherical powders pre-coated with 1 wt.% carbon nanoparticles by low-energy ball milling. Graphite flakes are used as carbon source, which aids powder flow during mixing as lubricant. Graphite transforms to nano-crystallite carbon during mixing which is favourable for the rapid formation of TiC second phase in the following SPS process. The composites exhibited a novel honeycomb-like cellular microstructure with the formation of 5-6 vol.% fine TiC submicron grains interconnected in the titanium α/β matrix. In addition, the reinforcement of the TiC phase with a nano-hardness of 12.4 GPa, improves the wear resistance of the parent alloy matrix (5.1 GPa), with a reduction of 26-28 % in wear rate during dry reciprocating sliding tests against Si_3N_4 balls. During sliding, the wear debris (predominantly anatase TiO_2) builds up on the raised TiC hard phase forming a barrier layer of adhered oxide that can protect the alloy matrix underneath from abrasion and oxidation, leading to a reduced wear rate.

Keywords	Titanium Matrix Composites; Powder Processing; SPS; Graphite; TiC; Wear.

Corresponding Author	Mingwen Bai
Order of Authors	Mingwen Bai, Righdan Namus, Yidong Xu, Dikai Guan, William Rainforth, Beverley Inkson

Suggested reviewers	Tanvir Hussain, Robert J K Wood, Anne Neville

Submission Files Included in this PDF

File Name [File Type]

Cover letter.doc [Cover Letter]

Response letter.docx [Response to Reviewers]

Highlights.docx [Highlights]

Graphitic Abstract.tif [Graphical Abstract]

Revised Manuscript.doc [Manuscript File]

Fig. 01.tif [Figure]

Fig. 02.tif [Figure]

Fig. 03-new.tif [Figure]

Fig. 04.tif [Figure]

Fig. 05-new.tif [Figure]

Fig. 06.tif [Figure]

Fig. 07.tif [Figure]

Fig. 08-new.tif [Figure]

Fig. 09-new.tif [Figure]

Fig. 10-new.tif [Figure]

Fig. 11.tif [Figure]

Fig. 12.tif [Figure]

Fig. 13.tif [Figure]

Fig. 14.tif [Figure]

Fig. 15-new.tif [Figure]

authorconfirm.doc [Author Agreement]

To view all the submission files, including those not included in the PDF, click on the manuscript title on your EVISE Homepage, then click 'Download zip file'.

Prof. Beverley J Inkson
NanoLAB Centre
Dept of Materials Science & Engineering
The University of Sheffield
Mappin Street, Sheffield, S1 3JD, UK
Tel: 0044 114 222 5925

24/06/2019

Dear Prof. Dienwiebel,

We thank the handling editors and the reviewers for their time and effort in reviewing our revised manuscript (WEA_2019_234_R1). The valuable comments and positive feedbacks have been greatly appreciated. In this revised version, we have carefully addressed the minor issues raised in the reviewer's comments, and made revisions accordingly (in red).

Please find our response letter and revised manuscript attached.
We look forward to your decision on the manuscript.

Sincerely,

Beverley J Inkson

Reviewer: 1

The revised version of manuscript is suitable for publishing.

Reviewer 2

Thank you for answering all the previous questions. I still have a minor revision, a question and a suggestion for future works:

i) The revision is as follows: "The formation of the grooves and localised wear debris regions within the wear track are PROBABLY associated with the experimentally recorded fluctuations in interfacial friction visible in the COF curves (Fig. 10)."

Response: Thank you for the valuable comment. Revision is made accordingly in section 4.3.

ii) About the question: In many tribological systems, it is interesting to obtain a fine carbide distribution. I think the honeycomb structure is homogeneously distributed at the macroscopic level, but comparing to other works you mentioned, can you affirm that it is also homogeneous at the microscopic level?

Response: As far as we can see, the carbide distribution is dependent on the morphology of the pre-coated carbon layer on the Ti64 powder surface, which we can affirm that has completely transformed to TiC phase after the reactive SPS process based on our SEM, EBSD and Raman results. Therefore, the carbide distribution may be less homogeneous at the microscopic level down to the Ti64 cellular size range as occasionally there were areas with less or no carbon coated on the Ti64 powder surface (Fig. 2), which led to discontinuity of the TiC cellular boundaries phase (Fig. 5).

iii) My suggestion for future works:

The increase of wear resistance with the presence of hard particle is expected since it is well discussed in literature. Maybe it would be more interesting to compare, in a future work of your group, the wear behavior of honeycomb structured material with other TiC reinforced TMC (from carbon nanotubes, carbon fiber cloth, and graphene) and also with materials which the manufacturing processes had been directly involved with conventional mechanical blending or ball milling.

Response: Thanks for the valuable suggestion. Yes. We agree that it is worth further investigating on the effect of our unique honeycomb structure on the wear behaviour comparing to other TiC reinforced TMC, in particular on the exact effects of carbide concentration and distribution.

- A new powder-based process to produce TiC reinforced Titanium Matrix Composites
- Ti spherical powders are pre-coated by graphite flakes as carbon source/flow aid
- Honeycomb-like cellular microstructure TiC 2nd phase forms during in-situ reaction
- Enhanced wear resistance due to the reinforcement of the TiC hard phase (12.4 GPa)
- Wear debris builds up on the raised TiC hard phase forming a protective barrier layer

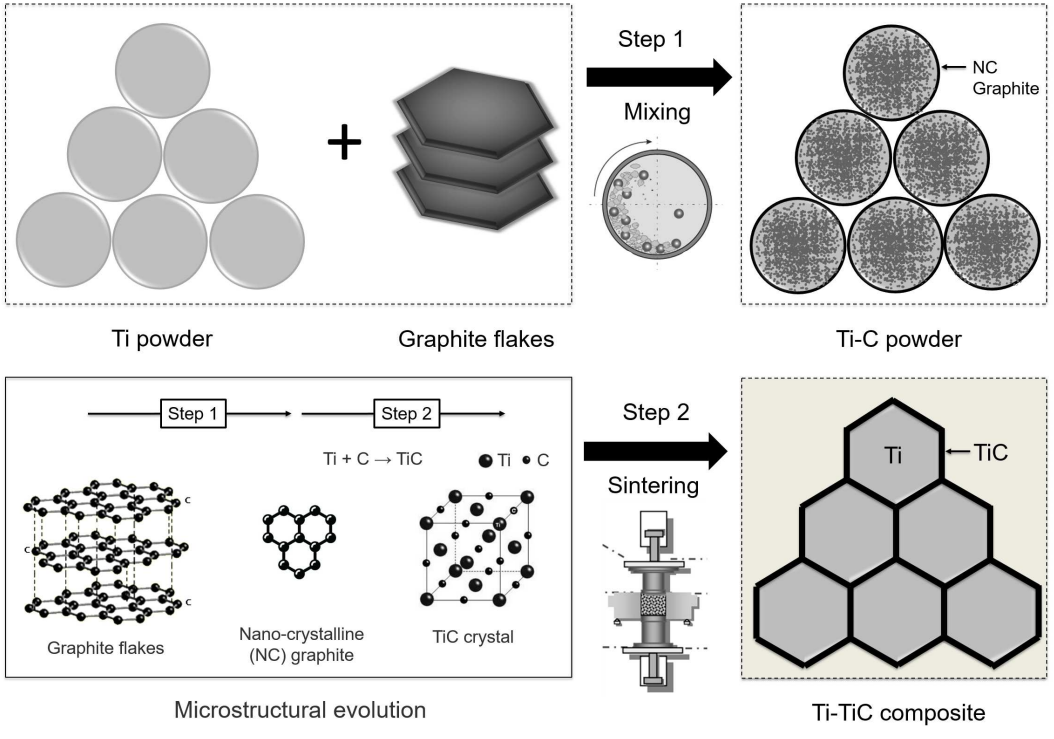
Step 1
Mixing
NC
Graphite
Ti powder
Graphite flakes
Ti-C powder
Step 1
Step 2
Ti + C → TiC
Ti
C
Graphite flakes
Nano-crystalline
(NC) graphite
TiC crystal
Step 2
Sintering
Ti
TiC
Microstructural evolution
Ti-TiC composite

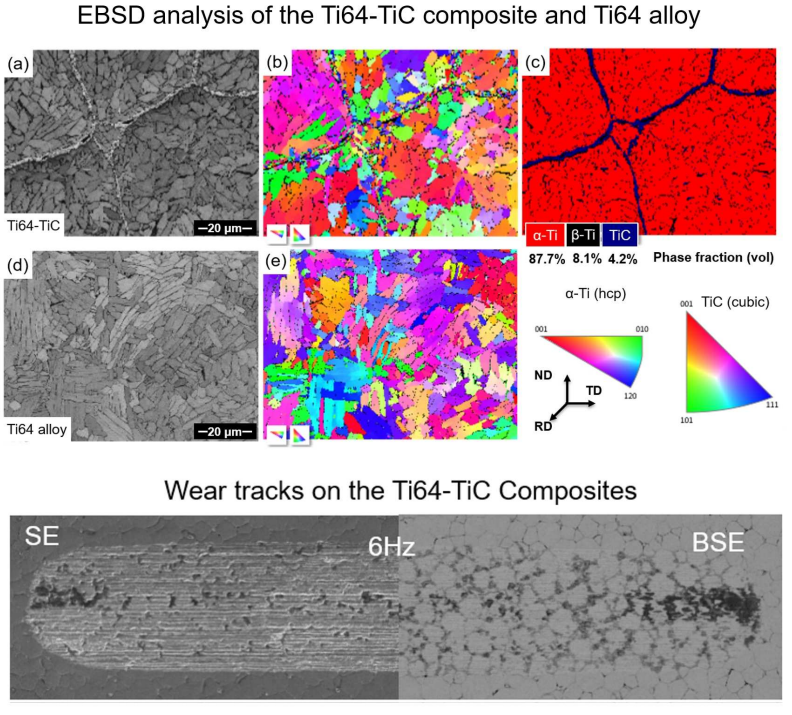
EBSD analysis of the Ti64-TiC composite and Ti64 alloy
(a)
(b)
(c)
Ti64-TiC
20 μm
α-Ti
β-Ti
TiC
87.7% 8.1% 4.2%
Phase fraction (vol)
α-Ti (hcp)
TiC (cubic)
(d)
(e)
Ti64 alloy
20 μm
ND
TD
RD
Wear tracks on the Ti64-TiC Composites
SE
6Hz
BSE

In-situ Ti-6Al-4V/TiC Composites Synthesized by Reactive Spark Plasma Sintering: Processing, Microstructure, and Dry Sliding Wear Behaviour

Mingwen Bai*, Righdan Namus, Yidong Xu, Dikai Guan, Mark W Rainforth, Beverley J Inkson*
Department of Materials Science and Engineering, The University of Sheffield, Sheffield, S1 3JD, UK
*Corresponding author Email: m.bai@sheffied.ac.uk; beverley.inkson@sheffield.ac.uk

Abstract: Titanium carbide (TiC) reinforced Titanium Matrix Composites (TMCs) have been synthesized via an in-situ reactive spark plasma sintering (SPS) process using commercial Ti-6Al-4V spherical powders pre-coated with 1 wt.% carbon nanoparticles by low-energy ball milling. Graphite flakes are used as carbon source, which aids powder flow during mixing as lubricant. Graphite transforms to nano-crystallite carbon during mixing which is favourable for the rapid formation of TiC second phase in the following SPS process. The composites exhibited a novel honeycomb-like cellular microstructure with the formation of 5-6 vol.% fine TiC submicron grains interconnected in the titanium α/β matrix. In addition, the reinforcement of the TiC phase with a nano-hardness of 12.4 GPa, improves the wear resistance of the parent alloy matrix (5.1 GPa), with a reduction of 26-28 % in wear rate during dry reciprocating sliding tests against Si_3N_4 balls. During sliding, the wear debris (predominantly anatase TiO_2) builds up on the raised TiC hard phase forming a barrier layer of adhered oxide that can protect the alloy matrix underneath from abrasion and oxidation, leading to a reduced wear rate.

Keywords: Titanium Matrix Composites; Powder Processing; SPS; Graphite; TiC; Wear.

1. Introduction

Titanium matrix composites (TMCs) have shown great potential in a wide range of applications including aerospace, automobiles and biomedicine owing to their improvement in strength,

creep resistance and wear resistance over Titanium alloys [1-4]. A selection of candidates for TMC reinforcements have already been investigated including SiC, Si_3N_4, Al_2O_3, TiC, TiN, and TiB [5-10]. Amongst these reinforcements, TiB and TiC exhibit outstanding chemical stability and compatibilities with the Ti matrix due to their similar density (Ti: 4.51, TiB: 4.57, TiC: 4.91 g/cm^3) [11] and coefficient of thermal expansion (CTE, 7.2 X 10^{-6} K^{-1} for TiB and TiC, 8.2 X 10^{-6} K^{-1} for Ti matrix [12, 13]). In most cases, these reinforcements have been directly added as particles to the metallic powders by conventional mechanical blending or ball milling. By mixing particles, however, it is difficult to achieve a homogeneous composition especially when adding nano-particles which have a high tendency for agglomeration [14, 15]. Moreover, conventional mechanical mixing of Ti powders with TiC or TiB hard particles can cause pronounced flattening of the soft Ti powder particles [16]. This usually leads to reduction in powder flowability when such composite powders are used as feedstock for a series of materials forming processes including powder-bed fusion, thermal spray, and cold deposition. To avoid these issues, recent studies on TMCs have introduced an in-situ fabrication method by adding carbon or boron reactants in the Ti-matrix to form TiC or TiB phase through the chemical reaction during the forming process [16-19]. This can achieve fine dispersion of the ceramic reinforcement and offer good control of the particle-matrix interface.

Considering the TMCs reinforced by in-situ TiC formation, a selection of carbon reactants have been added to Ti-alloy including carbon nanotubes, carbon fibre cloth, and graphene [20-23]. In this study, we offer an alternative route to prepare TiC reinforced TMC using graphite flakes, which are widely used as a cheap solid lubricant. The addition of graphite flakes to Ti-alloy powders during processing is also expected to aid the powder flow, and thereby minimize the deformation of Ti powder particles when using a low-energy ball milling process. The carbon-coated precursor composite powders are used as feedstock to form TiC phase by in-situ reacting with Ti matrix via spark plasma sintering (SPS) as an efficient method to produce TMC [24, 25]. Here the fabrication, microstructural characterization and dry sliding wear behaviour of the in-situ TiC reinforced TMCs have been evaluated, and wear mechanisms discussed.

2. Experimental

2.1. Powder mixing

A commercial Ti-6Al-4V powder (hereafter referred to as Ti64 powder, PREP®, TIMET, UK) with a perfectly spherical shape and a nominal size distribution of 106 ± 44 μm has been used in this study. This particle size is suitable for powder metallurgy (e.g. hot isostatic pressing and SPS), whereas it is too coarse for powder-bed additive manufacturing or powder injection moulding [26]. The Ti64 powder was mixed with 1 wt% of graphite flakes (99%, metals basis, Alfa Aesar, USA) with a flake diameter of 7-10 μm in a planetary ball mill (PM100, RETSCH GmbH, Germany) at a speed of 300 rpm for 1-8 hours with 30 min cooling per hour.

2.2. Spark plasma sintering process

The composite powder was loaded into a cylindrical graphite die (Φ 20 mm) with interfacial graphite foils to avoid welding and obtain a more uniform current flow. The pre-pressed powder was sintered by SPS (FCT Systeme GmbH, HP D1050, Germany) under vacuum at a 1000 ºC with a heating rate of 100 °C/min followed by a dwell time of 5 min and a maximum uniaxial pressure of 80 MPa to achieve the highest density. These processing conditions were chosen based on the results of preliminary experiments. The SPS processed materials are hereafter referred to as Ti64-TiC composite; while the Ti64 powder was also processed by SPS with the same conditions, and is referred to as Ti64 alloy for comparison.

2.3. Materials Characterization

The morphology and microstructure of the powder and the composite samples were examined by a field emission gun scanning electron microscopy (FEG-SEM, Inspect F50, FEI, USA). The phase composition was identified by powder X-ray Diffraction (XRD, D2 Phaser, Bruker, Germany) using Cu-Kα radiation at 30 kV and 10 mA, a step size of 0.05°(2θ), a step time of 2 s between 20 and 90°(2θ), and all data collected at 25 °C. Quantitative Rietveld refinement (TOPAS V5 software package) was used to determine the composition of TiC and α-Ti phase in the Ti64-TiC composite based on the XRD patterns. Electron backscatter diffraction (EBSD) was performed on a FEG SEM (7100F, JEOL Ltd., Japan) at an accelerating voltage of 15 kV.

EBSD scans were carried out using AZtechHKL software (Oxford Instruments, UK) with a step size of 0.1 μm. Elastic modulus and hardness of the Ti64 powder on polished cross-sections, the TiC phase and the Ti64-matrix were measured by a nano-indentation (Triboscope, Hysitron, USA) equipped with a Berkovich diamond tip at 10 mN load. Micro-hardness was measured by DuraScan hardness tester (Struers, USA) under 1N load. Raman spectra were acquired using a Renishaw InVia Raman Microscope with 50x objective at an excitation wavelength of 514 nm at ambient condition in extended mode ranging from 100 to 3500 cm^{-1}.

2.4. Reciprocating wear tests

Tribological tests were carried out on a UMT-2 TriboLab (Bruker, USA) at room temperature 20-25 °C, relative humidity 50-60%, unlubricated, and under an ambient atmospheric condition. All sample surfaces were polished down to mirror-like surfaces by using a colloidal silica suspension, and carefully cleaned in an isopropanol ultrasonic bath before wear tests. For the reciprocating sliding tests, a ball on plate configuration, which conformed to ASTM G133, was used with parameters: normal load of 0.5 N, sliding stroke of 2.5 mm at 6Hz and 1Hz, and total sliding distance of 54 m. The loading condition applied in this study corresponds to an initial Hertzian contact pressure of 537 MPa and a maximum shear stress of 161 MPa.

During the sliding tests, the dynamic coefficient of friction (COF) was recorded as a function of time by the servo-controlled normal load and lateral load on the DFM-0.5 loading cell (0.05 to 5 N) with a resolution of 0.25 mN. At least two tests were conducted at each test condition, and the averaged specific wear rates are reported. The number of repeated tests was determined by the repeatability of the COF measurements, i.e. if the measured COF varied significantly between two tests, then further repeated measurements (up to 3) were carried out to evaluate the statistical spread. Si_3N_4 ceramic balls (TSN-03NH, Grade 5) with a diameter of 4 mm (± 0.0013 mm) and a maximum surface roughness (Ra) of 0.02 μm were chosen as counter-faces for sliding tests. Si_3N_4 balls were used because of their minimum damage in comparison with other types of ball materials including Al_2O_3, stainless steel, and ZrO_2 after identical trial sliding tests against Ti64 base alloys. Wear volumes of the disk samples and the counter-face Si_3N_4

balls were measured by an 3D optical profilometer (Contour GT Bruker, USA). The surface morphology and the composition of the wear debris in the wear track were analysed by SEM equipped with energy dispersive spectroscopy (EDX, Oxford Instruments, UK).

3. Results

3.1. Ti64 and graphite composite powder

Typical morphology of the starting Ti64 powder and graphite flakes are shown in Fig. 1. The Ti64 powders have spherical shape and smooth surfaces (Fig. 1 (a, b)) with minimal satellite particles (Fig. 1 (a) arrowed). The graphite flakes exhibit typical plate-like morphology and a lamellar structure (Fig. 1 (c, d)). After mixing by planetary ball mill for 8 h, it is observed that the graphite flakes were completely coated onto the Ti64 powders surfaces (Fig. 2 (a, b)) with no excess left or adhered to the wall of the powder container. The Ti64 particles were coated with ~50% surface coverage of carbon clusters comprising predominantly nano-particles with a size of <100 nm (Fig. 2 (c, d)). Occasionally Ti64 particle satellites (as marked by white arrow in Fig. 2 (a)) can be observed, which cause lower coverage of carbon in the vicinity of the particle-particle junctions as indicated by the contrast. In addition, the mixing process was sufficiently mild so that the Ti64 powders retained their spherical shapes without any severe deformation, which will ensure a good powder flowability in subsequent processing.

The phase change of the composite powder after mixing was examined by XRD (Fig. 3). After both 4 h and 8 h mixing, the composite powder only exhibits XRD peaks of the constituent powders indicating no significant chemical reactions (e.g. oxidation or TiC formation) occurred during mixing. Compared to the starting powders, however, it is noticeable that the crystalline graphite peak (marked by shaded area in Fig. 3) in the XRD pattern became weaker and narrower after 4 h ball milling, and then completely disappeared after 8 h milling. This indicates that the starting graphite flakes are gradually transformed to near-amorphous nanoparticles during the powder mixing. After 8 h ball milling, no excess graphite flakes remained in the composite powder, which is consistent with the SEM observations of the composite (Fig. 2).

The microstructural evolution of graphite during mixing was further examined by Raman Spectroscopy (Fig. 4). After 8 h mixing, the Ti64-Graphite composite powder shows the appearance of a prominent band around 1350 cm^{-1}, which is known as the carbon D band (Fig. 4 (a)). This band is often referred to as the disorder band or the defect band as opposed to the carbon G or G' band as always seen in graphite and graphene. The formation of the disordered structure indicates that during powder mixing, the original ordered graphite flakes transformed to partially disordered nano-crystalline graphite corresponding to the nano-particles as observed in Fig. 2 (d). This transformation to nano-crystalline carbon can also be confirmed by the increase of the *I*(D)/*I*(G) peak intensity ratio, and the up-shift of G-position with peak deconvolutions of G1 and G2 indicting two varying degrees of disorder (Fig. 4 (b)).

3.2. Ti64-TiC composite microstructure

The microstructure of theTi64-TiC composite after SPS consolidation of the composite powder containing 1 wt.% of graphite was examined by SEM under both SE and BSE modes (Fig. 5). In SEM, a novel honeycomb-like microstructure is observed with two distinctive phases: (1) Ti64 matrix and (2) TiC phase with a brighter contrast in SE (Fig. 5 (a-c)). In cross-section, the TiC phase is interconnected in a grain-boundary-like structure with a ribbon-like shape and a width of 1-3 μm. The honeycomb microstructure is consistent with a 3D TiC-Ti64 cellular morphology, with cell dimensions inherited from the original Ti64 particles (Fig. 2). The mean diameter of the angular cells in the composites is 80 ± 14.0 μm as measured by SEM imaging analysis. Compared to the original Ti64 particle sizes of 106 ± 45 μm, a reduction of 24-25 % in size is observed as the result of the compression and densification of the powders during the SPS process. Additionally, the TiC cell boundaries have straight morphologies compared to the curved carbon coating on the original enveloped particles. The interface between the Ti64 matrix and TiC phase is seen to be coherent with no cracks and defects (Fig. 5 (c)).

In Fig. 5 (d), the cellular-morphology TiC phase is embedded in the Ti64 matrix which has mixed α/β grains exhibiting a microstructure of equiaxed (or globular) α-grains (grey) within a β-matrix. The β-phase appears to be brighter than α under BSE imaging due to the enrichment of

Vanadium. More detailed grain microstructure can be revealed from the EBSD analysis of the Ti64 α/β matrix together with the new formed TiC phase (Fig.6 (a-c)), in comparison to that of the parent Ti64 alloy (Fig.6 (d, e)). Fine TiC grains (Fig. 6 (b), blue colour) with a phase volume of 4.2 % and a grain size of 1-2 μm were identified in the TiC phase layer surrounding the Ti64 cells, which themselves exhibited different crystallographic variants throughout the Ti64 α/β-phase matrix. Here, the modification of the Ti64 grain microstructure does not have significant effect on its mechanical properties either at micro or nano-scale. The nano-hardness of the Ti64 matrix is 5.0 GPa for the Ti64-TiC composite and 5.1 GPa for the Ti64 alloy only, as measured by nano-indentation at a load of 10 mN. The micro-hardness of both Ti64 matrices is in the range of 340-380 HV. On the other hand, nano-indentation of the TiC boundary phase gives a nano-hardness of 12.4 GPa, which is nearly three times that of the Ti64 alloy matrix. Therefore, the honeycomb/cellular structure of the hard TiC phase enveloping the softer “cells” of Ti64 will strongly affect the composites’ mechanical/wear behaviour. This is supported by the evidence as shown in Fig. 7 of the surface of the as-polished Ti64-TiC composites. The TiC phase forms topographic crests with an overall surface roughness of 0.2 μm, due to slower polishing of the harder TiC ceramic phase resulting in a raised surface profile compared to the surrounding Ti64 matrix, which can also be observed by the image contrast in Fig. 5.

Quantitative Rietveld refinement of the XRD spectra (Fig. 8) calculates that the Ti64-TiC composite comprises 7.0 wt.% TiC phase, corresponding to 6.4 vol.%, assuming the density is 4.51 g/cm^3 for Ti64 matrix and 4.91 g/cm^3 for TiC phase [11]. This is slightly higher than the theoretical value, which is maximum 5 wt% TiC by adding 1 wt% of carbon in Ti64 according to the stoichiometric C/Ti ratio of 1:1. This may arise because TiC phase is a typical interstitial carbide, which is generally stable over a range of C/Ti compositional ratio from 0.5 to 1 [27], which would give rise to 5-9 wt% of TiC phase and match well with the XRD analysis. The lattice parameters were also retrieved from the Rietveld Refinement analysis. The c/a ratio in the α-phase (1.61) and the lattice parameter of *a* in the β-phase (3.23 Å) of the Ti64-TiC composite is 1-2 % higher than those of the SPS processed Ti64 alloy (1.59 and 3.21 Å,

respectively) under the same conditions indicating a minor incorporation of carbon into the α-Ti phase as random solid solution expanding the lattice structure during the SPS process.

3.3. Dry sliding wear behaviour of the Ti64-TiC composites

Fig. 9 summarizes the specific wear rates of the Ti64-TiC composite in comparison to the Ti64 alloy at two speeds (6Hz and 1Hz corresponding to 30 mm/s and 5 mm/s, respectively). It is evident that the higher speed at 6Hz accelerated the wear rates of both balls and disks compared to the lower speed at 1Hz. Also, in comparison to the wear rates of the Ti64 alloy, a clear reduction of 26-28 % in specific wear rates is found for Ti64-TiC composites at both speeds. In Fig. 9, the wear rates of Si_3N_4 balls are also presented using the right y-axis with values of two orders of magnitude lower. The wear of the Si_3N_4 balls was over 50% slower on the composite than on the Ti64 alloy at both speeds. The recorded COF values did not show measurable difference in friction between the Ti64 alloy and the Ti64-TiC composite at these two speeds (Fig. 10), while repeated short-term fluctuations are observed in all COF curves.

To evaluate the wear mechanism, further analysis was carried out to examine the wear tracks post mortem. Typical morphology and microstructure of the reciprocating wear tracks on the Ti64 alloy and Ti64-TiC composite after rubbing with a 4mm Si_3N_4 ball are shown in Fig. 11. Parallel grooves are identified in all wear tracks along the direction of ball movement for these two samples at both speeds. Patches of wear debris clusters can also be observed adhered on the surface of the wear tracks as indicated by regions of dark SE and BSE contrast. These debris “patches” are randomly distributed in the wear track of Ti64 alloy, but have a much more ordered distribution on the Ti64-TiC composite surfaces which matches perfectly with the dimensions of the “honeycomb” like microstructure of the TiC cells (Fig. 5-7). In addition, the wear tracks of both samples at the lower speed (1Hz) are seen to exhibit a relatively higher surface area of residual wear debris than those tested at the higher speed (6Hz).

Considering the chemistry of the wear track, BSE images and EDX mapping (Figs. 12 and 13) reveal that the “patches” are chemically distinct from the surrounding materials, consisting of oxides with an enrichment of Ti and Si originating from the Si_3N_4 balls. Typical morphology and

composition of wear debris nanoparticle clusters inside the wear track under BSE shows variable contrast: the darker phase regions have relatively higher Si content; while the brighter high BSE yield regions comprise predominantly Ti-rich oxide. More detailed compositional analysis measured by semi-quantitative EDX point analysis are shown in Tables 1 and 2.

Table 1. EDX point analysis on the worn surface of the Ti64 alloy (wt. %)

	b1	**b2**	**b3**	**c1**	**c2**	**c3**	**c4**	**c5**
Ti	61.0	63.5	41.3	85.7	63.5	43.4	47.9	46.5
O	27.4	23.9	43.9	0	23.7	44.0	41.0	42.8
Si	3.2	0.4	3.6	0	0.7	4.2	3.2	2.8
Al	2.9	4.1	3.2	6.3	4.1	2.8	2.8	2.6
V	2.3	3.3	1.9	3.8	2.5	1.9	1.8	1.8
C	3.2	4.9	6.2	4.3	5.4	3.6	3.2	3.4

Table 2. EDX point analysis on the worn surface of the Ti64-TiC composite (wt. %)

	b1	**b2**	**b3**	**c1**	**c2**	**c3**	**c4**	**c5**
Ti	58.9	51.0	72.4	85.7	54.6	62.6	52.7	68.4
O	30.8	39.9	17.7	0	37.1	27.2	38.3	21.4
Si	1.5	2.1	0.4	0	0.7	0.7	1.0	0.6
Al	3.8	3.2	4.1	6.2	3.2	4.0	3.4	3.0
V	2.5	2.0	2.5	2.2	2.2	2.6	1.9	2.7
C	2.5	1.7	2.8	5.9	2.2	2.8	2.7	4.0

The structure of the wear track also varies along its length, for example, near the track end where the sliding direction is reversed (Fig.12 (b) and 13 (b)) and in the middle of the track (Fig.12 (c) and 13 (c)). The end of stroke area has a higher content of nanoparticle debris

containing Si-rich oxide than the mid-stroke zone as the wear debris gradually accumulates during the reciprocating Si_3N_4 ball motion forming an oxide tribolayer build-up. The end-stroke debris is composed of nano-sized (100-300 nm) oxide globular particles (Fig. 12 (d) and 13 (d)). These wear debris on both samples comprised of predominantly TiO_2 throughout the wear tracks as indicated by the characteristic Raman peaks of TiO_2 anatase phase (Fig. 14), compared to the Raman spectra of the TiC phase and Ti64 matrix prior to wear testing.

4. Discussion

4.1. Powder processing

The results here have demonstrated a new method via in-situ SPS for the production of Ti64-TiC composites reinforced by interconnected TiC in a honeycomb-like cellular microstructure. The use of graphite flakes to pre-coat the Ti64 powder (feedstock) has shown several advantages over a selection of other carbon sources in previous literature that have been added into the Ti64 matrix for the in-situ formation of Ti64-TiC composite, e.g. multi-walled carbon nanotubes (MWCNTs) [20], vapour grown carbon fibres/nanotubes (VGCFs) [18, 22], and woven carbon fibre cloth [25]. Apart from the graphite's economically low cost and great availability, graphite flakes can also aid the powder flow during mixing as a lubricant and do not affect the alloy powder's original spherical shape, as shown in Figs. 1 and 2. Retention of spherical particles is very important to ensure good flowability for following processes.

The transformation from graphite flakes to nano-crystallite carbon during ball milling, as shown in Figs. 3 and 4, produces a fine dispersion of carbon nanoparticles on the Ti64 powder surface (Fig. 2). Nano-crystalline graphitic materials are conventional products of ball milling of graphite, with the introduction of defects into the crystallites prior to complete amorphisation [28]. This transformation is also favourable for the rapid formation of nano-crystalline TiC during the following SPS process owing to the increase of the carbon specific surface area [29]. All of these benefits from using graphite contribute to improved production efficiency (i.e. utilization of the raw materials, energy consumption, and time) as the addition of 1 wt.% graphite flakes in the Ti64 powder converts to 7 wt.% TiC after the fast in-situ SPS process (5 min at 1000 ºC).

4.2. In-situ SPS process

The resulting Ti64-TiC composite exhibited a unique honeycomb-like cellular microstructure with interconnected TiC grains forming boundaries separating discrete Ti64 cells (Figs. 5-8). The novel Ti64-TiC composite fabricated here exhibited better wear resistance compared to the parent Ti64 alloy with a 26-28% reduction in wear rate. The Ti64-TiC composites here also exhibit a distinct α/β grain microstructure in the Ti64 cells compared to the SPS Ti64 alloy processed under the same conditions (Fig. 6 (d, e)). The SPS Ti64 microstructure is typical of a β-processed Ti64 alloy with lath-like precipitates formed during fast cooling from above the β-transus temperature. In Fig. 6, the matrix of the Ti64-TiC composite however consists of more equiaxed (or globular) α-precipitates within a β-matrix rather than a predominantly laths (or lamellar) shape. The formation of equiaxed Ti-α phase in TMCs has also been observed by Hill et al. [30] in TiB reinforced Ti64 composites, and it was suggested that TiB precipitates can act as heterogeneous nucleation sites for equiaxed α formation during the cooling process.

4.3. Wear mechanisms

The dry sliding wear behaviour of both Ti64 alloy and Ti64-TiC composites are consistent with a combination of abrasion and adhesion, based on the experimental results and related investigations [31, 32]. It is evidenced by the deep parallel grooves in worn surfaces produced by ploughing, and adhesive clusters of wear debris present across the wear scar (Figs. 11-13). The observed 3rd body debris will arise from a number of mechanisms including direct abrasion of the Ti64 alloy/Ti64-TiC composite surfaces (and associated oxide layers) by the counter-face Si_3N_4 balls [33-35], adhesive wear processes between the Si_3N_4 balls and the alloy/composite surfaces, and complex follow-on 3rd body abrasion/adhesive wear processes involving the generated 3rd body wear debris within the reciprocating wear track. The formation of the grooves and localised wear debris regions within the wear track are probably associated with the experimentally recorded fluctuations in interfacial friction visible in the COF curves (Fig. 10).

For the novel honeycomb-like cellular microstructure Ti64-TiC composite produced in this study, key aspects of its wear mechanism are illustrated schematically in Fig. 15. First of all, the

presence of the cellular-structured hard TiC phase, with indentation hardness of 12.4 GPa, leads to a lower local penetration depth of the abrasive asperities when in contact, and ultimately a reduced abrasive wear rate. It was observed that after polishing the TiC cellular boundaries formed raised ridges up to 1 μm higher than the surrounding Ti64 matrix (Fig. 7), due to the differential TiC<Ti64 wear rate. In the vicinity of the raised TiC ridges, the direct contact between the Si_3N_4 hard counter body and the Ti soft matrix underneath will be reduced. Furthermore, the raised TiC ridges can trap surrounding wear debris forming a region of 3rd body debris which can act as a "protective barrier" to reduce direct wear of the Ti64 surface. This mechanism is evidenced by the formation of the honey-comb shape stripes of adhered debris layer in the wear track segregated at the underlying TiC phase (Fig. 13) as opposed to the randomly distributed "patches" found in the wear track of the Ti64 alloy (Fig. 12).

Considering the influence of oxidation on the tribology of Ti64 and Ti64-TiC composites, the high affinity of Ti to O_2 causes the formation of a very thin oxide layer on the surface of Ti64 alloys in air at room temperature [36]. Anatase TiO_2 was identified by Raman Spectroscopy in the wear debris on all sample surfaces after the wear process (Fig. 14). TiC phase can also be oxidized at temperatures above 300 ºC with the products of TiO_2 (anatase) and CO_2 [37]. In addition, TiC is more thermodynamically and kinetically stable than Ti64 alloy against oxidation. Huang et al. [38] demonstrated that the oxidation resistance of a Ti64-TiC composite was over 10% higher than that of the Ti64 alloy during isothermal oxidation at temperatures of 600-800 ºC. The slower growth of oxide on TiC compared to the Ti64 matrix may also contribute to the reduction of material loss during dry sliding leading to a lower wear rate for the composite.

5. Conclusions

This work has presented a new SPS-based process to prepare Ti64-TiC composites; and evaluated the resulting microstructure, phase distribution and wear behaviour. Specifically, spherical Ti64 powders were first ball-milled with 1 wt. % of graphite flakes forming a uniformly carbon coated composite powder while retained a good powder sphericity and flowability. The composite powders were consolidated by in-situ reactive SPS process, forming 5-6 vol % of

TiC phase within the Ti64 matrix. The TiC precipitates also promote equiaxed α-formation in the Ti64 matrix by acting as heterogeneous nucleation sites offering a potential of better resistance to crack growth/propagation. The composite exhibits a novel cellular microstructure consisting of 80 ± 14 μm cells of Ti64 alloy bonded by 1-3 μm thick TiC cell boundaries.

Dry reciprocating sliding test results demonstrated that the wear resistance of the cellular Ti64-TiC composite is superior to the Ti64 alloy with a reduction of 26-28 % in wear rate. The Ti64-TiC composite exhibits a wear/friction behaviour that is dominated by the oxidation of Ti-matrix and TiC phase during sliding forming adhered wear debris clusters or “patches” that consist of predominantly anatase TiO_2 in the wear track. It was found that the wear debris oxide built up alongside the raised TiC hard phase cell boundaries (with a nano-hardness of 12.4 GPa), forming a protective barrier against abrasion and oxidation to the Ti64 matrix underneath (5.1 GPa), and leading a significant reduction of wear rate of the SPS Ti64-TiC composite.

Acknowledgement

This work is supported by the Engineering and Physical Sciences Research Council (Grant number EP/R001766/1) as a part of ‘Friction: The Tribology Enigma’ (www.friction.org.uk), a collaborative Programme Grant between the Universities of Leeds and Sheffield. The authors thank Dr. Karen Alvey and Mr. Martin J. Roe from the Nanoscale and Microscale Research Centre (nmRC) in the University of Nottingham for EBSD analysis and technical assistance.

References

[1] I.Y. Kim, B.J. Choi, Y.J. Kim, Y.Z. Lee, Friction and wear behavior of titanium matrix (TiB+TiC) composites, Wear 271(9) (2011) 1962-1965.
[2] Y. Qin, L. Geng, D. Ni, Dry sliding wear behavior of extruded titanium matrix composite reinforced by in situ TiB whisker and TiC particle, Journal of Materials Science 46(14) (2011) 4980-4985.
[3] D. Gu, G. Meng, C. Li, W. Meiners, R. Poprawe, Selective laser melting of TiC/Ti bulk nanocomposites: Influence of nanoscale reinforcement, Scripta Materialia 67(2) (2012) 185-188.
[4] Y. Chen, J. Zhang, N. Dai, P. Qin, H. Attar, L.-C. Zhang, Corrosion Behaviour of Selective Laser Melted Ti-TiB Biocomposite in Simulated Body Fluid, Electrochimica Acta 232 (2017) 89-97.
[5] L.C. Zhang, H. Attar, Selective Laser Melting of Titanium Alloys and Titanium Matrix Composites for Biomedical Applications: A Review Advanced Engineering Materials 18(4) (2016) 463-475.
[6] A.P.I. Popoola, L. Phume, S. Pityana, V.S. Aigbodion, In-situ formation of laser Ti6Al4V–TiB composite coatings on Ti6Al4V alloy for biomedical application, Surface and Coatings Technology 285 (2016) 161-170.
[7] X. Zhang, F. Song, Z. Wei, W. Yang, Z. Dai, Microstructural and mechanical characterization of in-situ TiC/Ti titanium matrix composites fabricated by graphene/Ti sintering reaction, Materials Science and Engineering: A 705 (2017) 153-159.

[8] Q. An, L.J. Huang, Y. Bao, R. Zhang, S. Jiang, L. Geng, M. Xiao, Dry sliding wear characteristics of in-situ TiBw/Ti6Al4V composites with different network parameters, Tribology International 121 (2018) 252-259.
[9] H. Attar, S. Ehtemam-Haghighi, D. Kent, I.V. Okulov, H. Wendrock, M. B□nisch, A.S. Volegov, M. Calin, J. Eckert, M.S. Dargusch, Nanoindentation and wear properties of Ti and Ti-TiB composite materials produced by selective laser melting, Materials Science and Engineering: A 688 (2017) 20-26.
[10] P. Nandwana, J. Hwang, M. Koo, J. Tiley, S. Hong, R. Banerjee, Formation of equiaxed alpha and titanium nitride precipitates in spark plasma sintered TiB/Ti–6Al–4V composites, Materials Letters 83 (2012) 202-205.
[11] B.-J. Choi, I.L.Y. Kim, Y.-Z. Lee, Y.-J. Kim, Microstructure and friction/wear behavior of (TiB+TiC) particulate-reinforced titanium matrix composites, Wear 318(1) (2014) 68-77.
[12] S. Wei, Z.-H. Zhang, F.-C. Wang, X.-B. Shen, H.-N. Cai, S.-K. Lee, L. Wang, Effect of Ti content and sintering temperature on the microstructures and mechanical properties of TiB reinforced titanium composites synthesized by SPS process, Materials Science and Engineering: A 560 (2013) 249-255.
[13] G. Wen, S.B. Li, B.S. Zhang, Z.X. Guo, Reaction synthesis of TiB2–TiC composites with enhanced toughness, Acta Materialia 49(8) (2001) 1463-1470.
[14] W. Zhou, X. Sun, K. Kikuchi, N. Nomura, K. Yoshimi, A. Kawasaki, In situ synthesized TiC/Mo-based composites via laser powder bed fusion, Materials & Design (2018).
[15] W. Li, H. Assadi, F. Gaertner, S. Yin, A Review of Advanced Composite and Nanostructured Coatings by Solid-State Cold Spraying Process, Critical Reviews in Solid State and Materials Sciences (2018) 1-48.
[16] H. Attar, M. Bönisch, M. Calin, L.-C. Zhang, S. Scudino, J. Eckert, Selective laser melting of in situ titanium–titanium boride composites: processing, microstructure and mechanical properties, Acta Materialia 76 (2014) 13-22.
[17] M.Y. Koo, J.S. Park, M.K. Park, K.T. Kim, S.H. Hong, Effect of aspect ratios of in situ formed TiB whiskers on the mechanical properties of TiBw/Ti–6Al–4V composites, Scripta materialia 66(7) (2012) 487-490.
[18] S. Li, B. Sun, H. Imai, K. Kondoh, Powder metallurgy Ti–TiC metal matrix composites prepared by in situ reactive processing of Ti-VGCFs system, Carbon 61 (2013) 216-228.
[19] Y. Hu, B. Zhao, F. Ning, H. Wang, W. Cong, In-situ ultrafine three-dimensional quasi-continuous network microstructural TiB reinforced titanium matrix composites fabrication using laser engineered net shaping, Materials Letters 195 (2017) 116-119.
[20] B. Ya, B. Zhou, H. Yang, B. Huang, F. Jia, X. Zhang, Microstructure and mechanical properties of in situ casting TiC/Ti6Al4V composites through adding multi-walled carbon nanotubes, Journal of Alloys and Compounds 637 (2015) 456-460.
[21] G. Huang, Y. Han, X. Guo, D. Qiu, L. Wang, W. Lu, D. Zhang, Effects of extrusion ratio on microstructural evolution and mechanical behavior of in situ synthesized Ti-6Al-4V composites, Materials Science and Engineering: A 688 (2017) 155-163.
[22] P. Pripanapong, T. Mimoto, J. Umeda, H. Imai, K. Kondoh, Effect of vapor grown carbon fiber content on microstructure and tensile properties of Ti64/TiC composite fabricated by powder metallurgy method, Journal of Composite Materials 50(24) (2015) 3405-3414.
[23] W.-H. Wei, Z.-N. Shao, J. Shen, X.-M. Duan, Microstructure and mechanical properties of in situ formed TiC-reinforced Ti–6Al–4V matrix composites, Materials Science and Technology 34(2) (2018) 191-198.
[24] G. Olivier, G.-J. Jesus, D. Benjamin, K. Tobias, S. Gabi, R. Jan, H. Mathias, Field-Assisted Sintering Technology/Spark Plasma Sintering: Mechanisms, Materials, and Technology Developments, Advanced Engineering Materials 16(7) (2014) 830-849.
[25] Y. Hao, J. Liu, J. Li, S. Li, Q. Zou, X. Chen, Rapid preparation of TiC reinforced Ti6Al4V based composites by carburizing method through spark plasma sintering technique, Materials & Design (1980-2015) 65 (2015) 94-97.
[26] Y. Zeng, D. Wang, X. Xiong, X. Zhang, P.J. Withers, W. Sun, M. Smith, M. Bai, P. Xiao, Ablation-resistant carbide Zr0.8Ti0.2C0.74B0.26 for oxidizing environments up to 3,000 °C, Nature Communications 8(15836) (2017).
[27] E. Kusano, A. Satoh, M. Kitagawa, H. Nanto, A. Kinbara, Titanium carbide film deposition by DC magnetron reactive sputtering using a solid carbon source, Thin Solid Films 343-344 (1999) 254-256.
[28] D.E. Smeulders, A.S. Milev, G.S. Kamali Kannangara, M.A. Wilson, Rod milling and thermal annealing of graphite: Passing the equilibrium barrier, Journal of Materials Science 40(3) (2005) 655-662.
[29] H. Jia, Z. Zhang, Z. Qi, G. Liu, X. Bian, Formation of nanocrystalline TiC from titanium and different carbon sources by mechanical alloying, Journal of Alloys and Compounds 472(1) (2009) 97-103.

[30] D. Hill, R. Banerjee, D. Huber, J. Tiley, H.L. Fraser, Formation of equiaxed alpha in TiB reinforced Ti alloy composites, Scripta Materialia 52(5) (2005) 387-392.
[31] Z. Doni, A. Alves, F. Toptan, J. Gomes, A. Ramalho, M. Buciumeanu, L. Palaghian, F. Silva, Dry sliding and tribocorrosion behaviour of hot pressed CoCrMo biomedical alloy as compared with the cast CoCrMo and Ti6Al4V alloys, Materials & Design (1980-2015) 52 (2013) 47-57.
[32] M.O. Alam, A.S.M.A. Haseeb, Response of Ti–6Al–4V and Ti–24Al–11Nb alloys to dry sliding wear against hardened steel, Tribology International 35(6) (2002) 357-362.
[33] I.M. Hutchings, Ductile-brittle transitions and wear maps for the erosion and abrasion of brittle materials, Journal of Physics D: Applied Physics 25(1A) (1992) A212-A221.
[34] H. Dong, 3 - Tribological properties of titanium-based alloys, in: H. Dong (Ed.), Surface Engineering of Light Alloys, Woodhead Publishing2010, pp. 58-80.
[35] T.S. Eyre, Wear characteristics of metals, Tribology International 9(5) (1976) 203-212.
[36] H. Guleryuz, H. Cimenoglu, Oxidation of Ti–6Al–4V alloy, Journal of Alloys and Compounds 472(1) (2009) 241-246.
[37] S. Shimada, K. Mochidsuki, The oxidation of TiC in dry oxygen, wet oxygen, and water vapor, Journal of Materials Science 39(2) (2004) 581-586.
[38] L.J. Huang, L. Geng, Y. Fu, B. Kaveendran, H.X. Peng, Oxidation behavior of in situ TiCp/Ti6Al4V composite with self-assembled network microstructure fabricated by reaction hot pressing, Corrosion Science 69 (2013) 175-180.

Figure Captions

Fig. 1. SEM imaging of (a, b) Ti64 powder and (c, d) graphite flakes showing the morphology of the starting powder before mixing under low and high magnifications.

Fig. 2. SEM imaging of the composite powder after mixing showing retained spherical shapes, and an evenly distributed but discontinuous carbon layer comprising nanoparticles.

Fig. 3. Combined XRD patterns of the Ti64 powder, graphite flakes, and the Ti64-Graphite composite powder after 4h and 8h mixing. Graphite (002) peak is indexed in shaded area.

Fig. 4. Raman spectra of (a) the starting graphite flakes and the Ti64-Graphite composite powder after 8h mixing with shaded areas indexed as the D, G and G' band; and (b) detailed peak deconvolutions of G band showing the shift of the G-position after mixing.

Fig. 5. SEM imaging of the Ti64-TiC composite microstructure under SE (a, b, and d) and BSE (c and e), together with the Ti64 alloy microstructure under BSE (f) as a comparison.

Fig. 6. EBSD analysis of (a-c) Ti64-TiC composites and (d, e) Ti64 alloy: (a, d) band contrast maps; (b, e) normal direction inverse pole figure (ND-IPF) colour maps; (c) phase maps.

Fig. 7. Surface morphology of the as-polished Ti64-TiC composite sample prior to the wear testing measured by 3D optical interferometry showing the topography of the surface with a measured roughness Ra of 0.215 μm due to the "ridge-like" raised TiC-phase.

Fig. 8. Combined XRD patterns of the Ti64-TiC composite and the Ti64 alloy. The inset values are the results of Rietveld refinement showing the calculated phase compositions.

Fig. 9. Specific wear rates of the Ti64-alloy and Ti64-TiC composite sample disks (y-axis on the let) and the Si_3N_4 ball (y-axis on the right) at load of 0.5 N and speeds of 6Hz and 1Hz.

Fig.10. Coefficient of friction (COF) measured as a function of sliding cycles of the Ti64-alloy and Ti64-TiC composite at load of 0.5 N and speeds of (a) 6Hz and (b) 1Hz.

Fig. 11. SE and BSE imaging of the surface morphology of the wear track in the Ti64 alloy and Ti64-TiC composites after 10800 sliding cycles at load of 0.5 N and speeds of 6Hz and 1Hz.

Fig. 12. BSE images and corresponding EDX maps of O, Si, Ti and Al, showing the microstructure and composition of the debris in the wear tracks (centre and edge) of the Ti64 alloys after 10800 sliding cycles at load of 0.5 N and speeds of 6Hz.

Fig. 13. BSE images and corresponding EDX maps of O, Si, Ti and Al, showing the microstructure and composition of the debris in the wear tracks (centre and edge) of the Ti64-TiC composite after 10800 sliding cycles at load of 0.5 N and speeds of 6Hz.

Fig. 14. Raman spectra of the wear debris identified as TiO_2 anatase, in comparison with the Si_3N_4 phase in the ball and the TiC phase in the Ti64-TiC composite prior to the wear testing.

Fig. 15. Schematic drawing to illustrate the wear mechanism of Ti64-TiC composites.

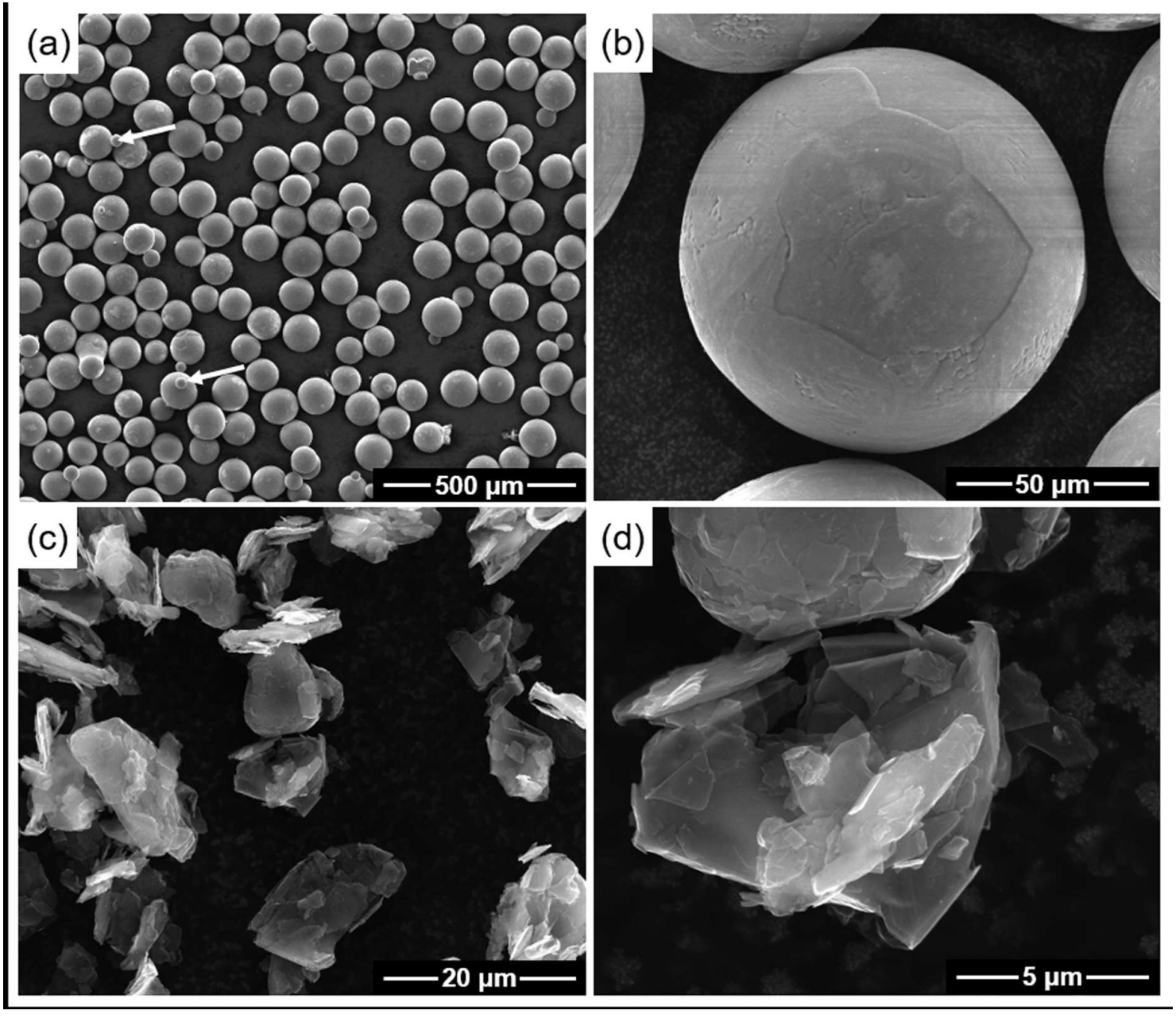
(a)
500 µm
(b)
50 µm
(c)
20 µm
(d)
5 µm

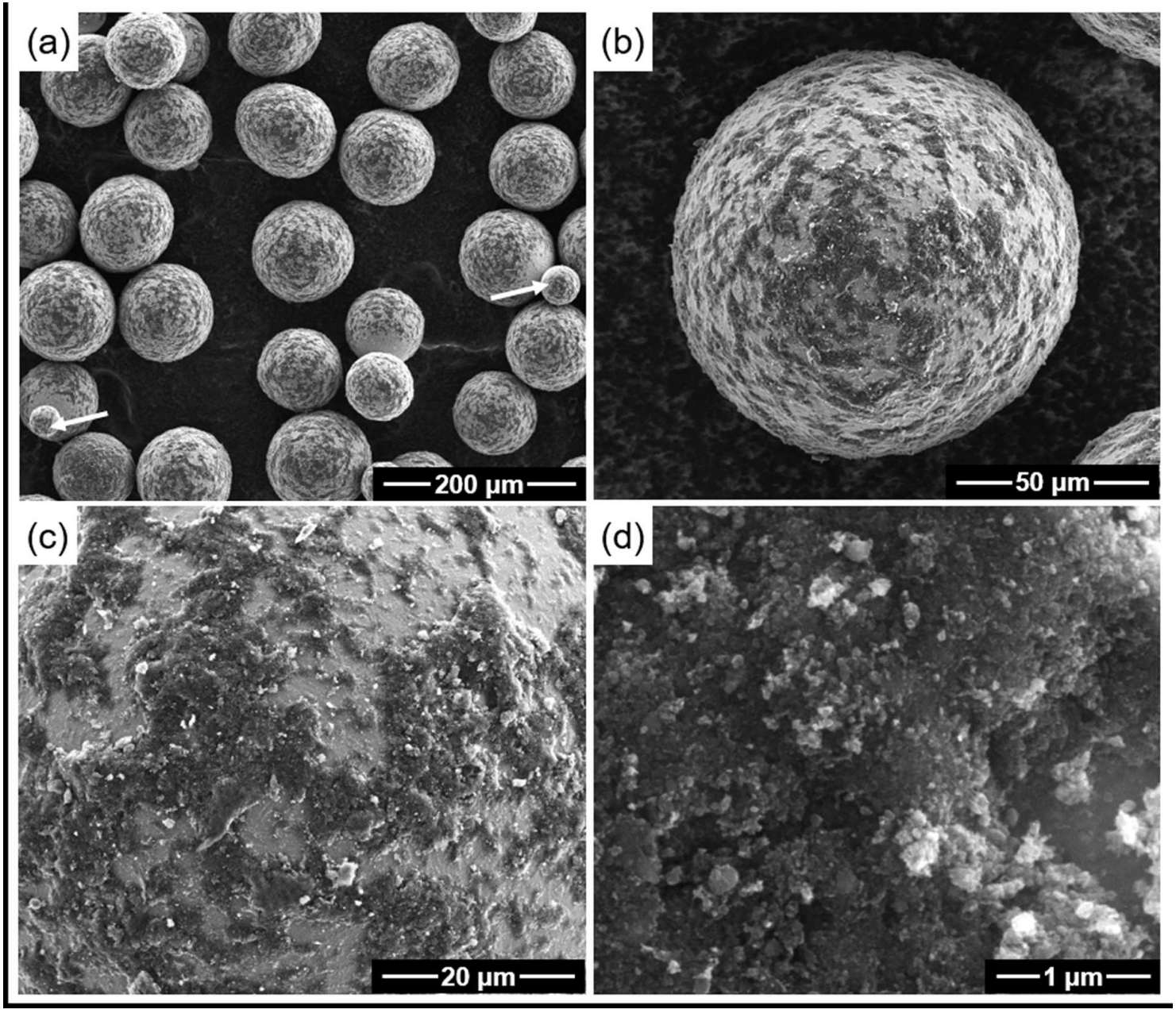
(a)
200 µm
(b)
50 µm
(c)
20 µm
(d)
1 µm

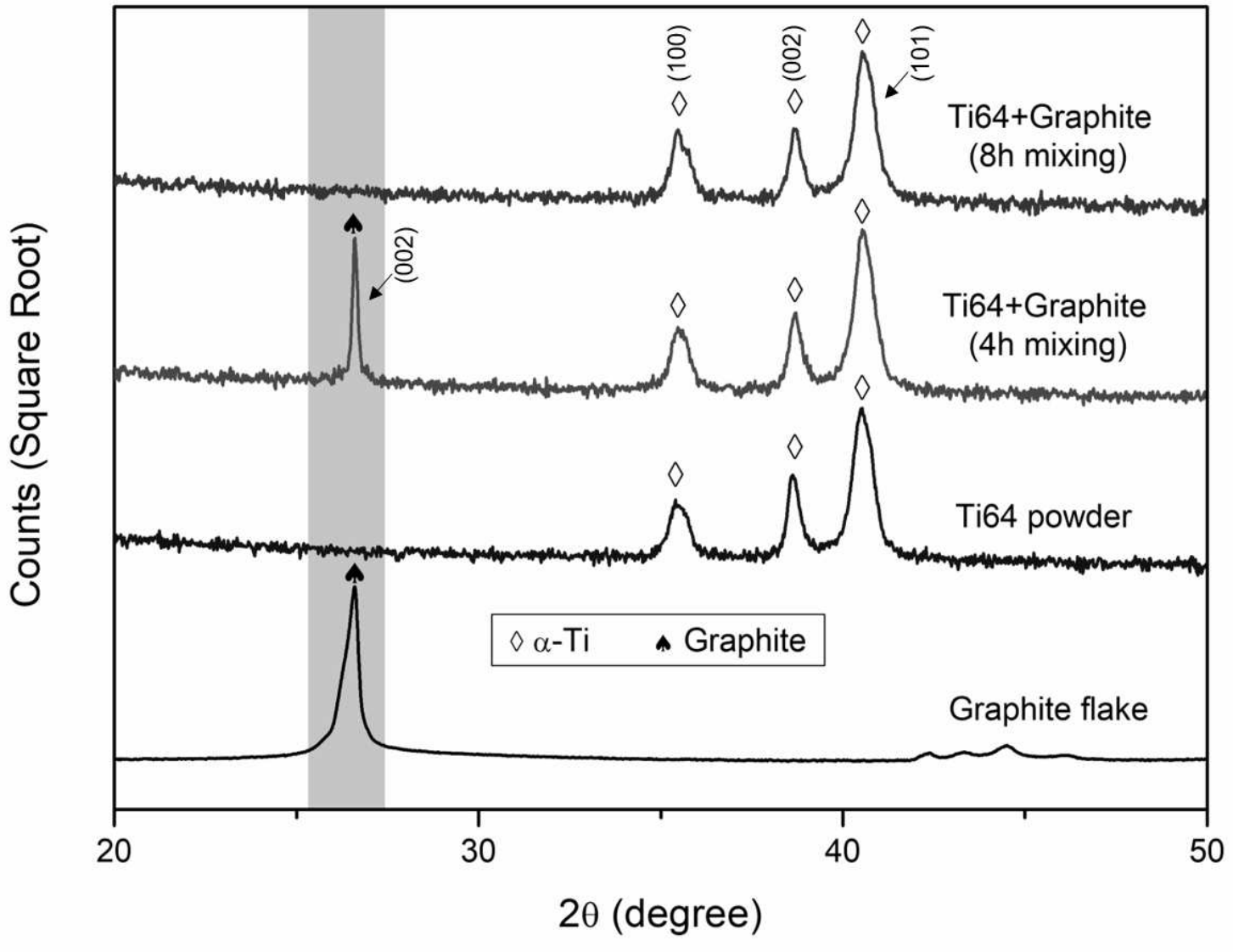
Counts (Square Root)
(100)
(002)
(101)
Ti64+Graphite
(8h mixing)
(002)
Ti64+Graphite
(4h mixing)
Ti64 powder
◊ α-Ti
♠ Graphite
Graphite flake
20
30
40
50
2θ (degree)

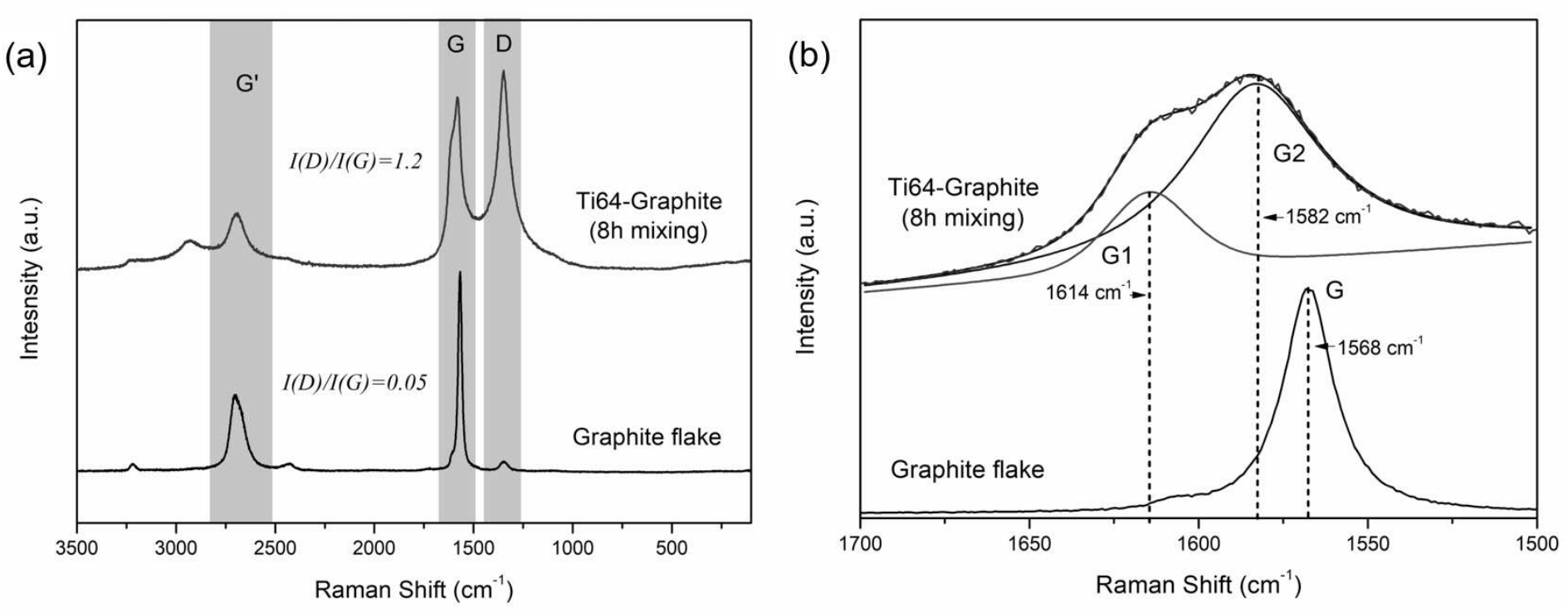
(a)
G'
G
D
I(D)/I(G)=1.2
Ti64-Graphite
(8h mixing)
I(D)/I(G)=0.05
Graphite flake
Intesnsity (a.u.)
3500
3000
2500
2000
1500
1000
500
Raman Shift (cm-1)
(b)
Ti64-Graphite
(8h mixing)
G2
1582 cm-1
G1
1614 cm-1
G
1568 cm-1
Graphite flake
Intensity (a.u.)
1700
1650
1600
1550
1500
Raman Shift (cm-1)

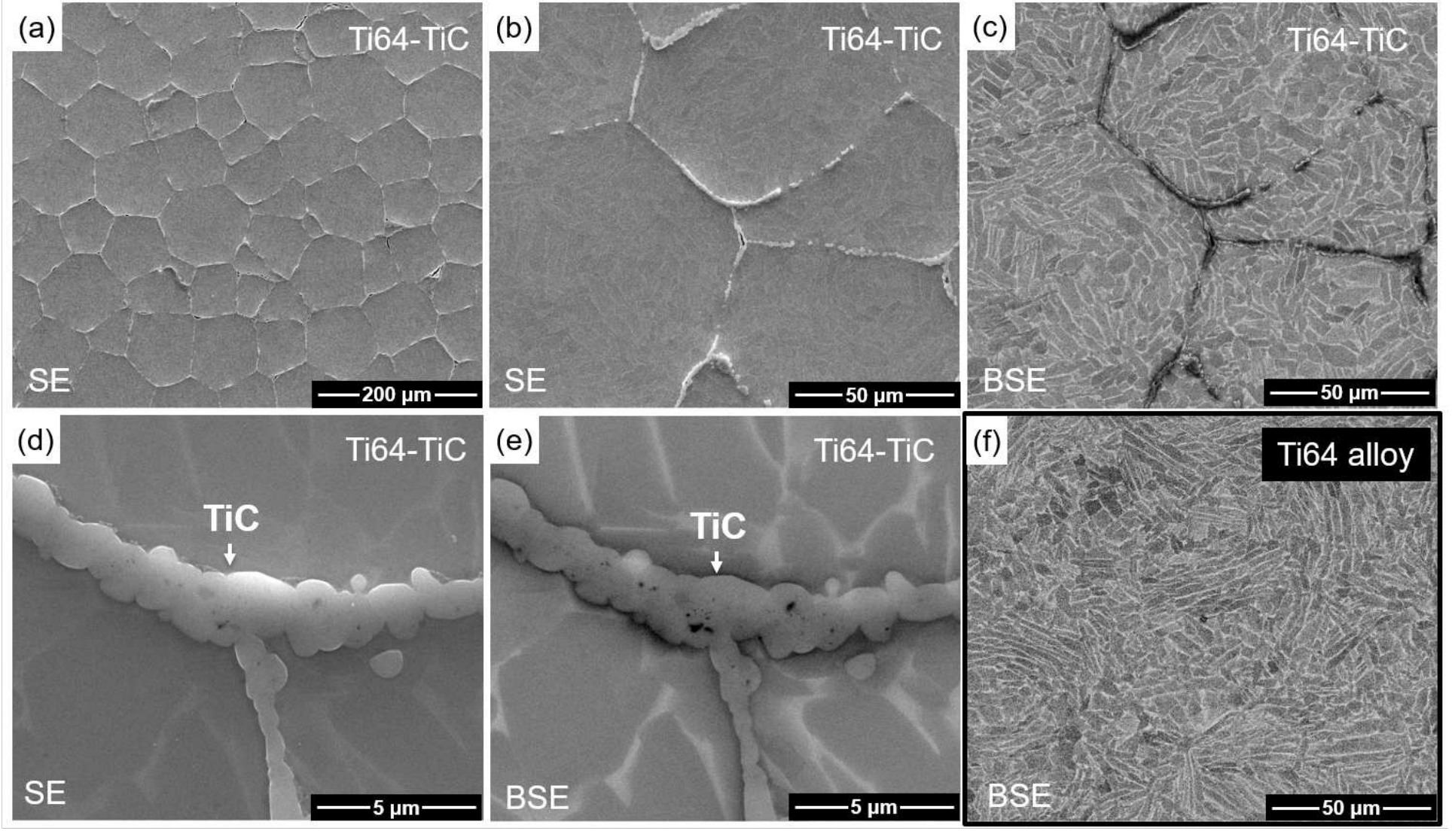
(a)
Ti64-TiC
SE
200 μm
(b)
Ti64-TiC
SE
50 μm
(c)
Ti64-TiC
BSE
50 μm
(d)
Ti64-TiC
TiC
SE
5 μm
(e)
Ti64-TiC
TiC
BSE
5 μm
(f)
Ti64 alloy
BSE
50 μm

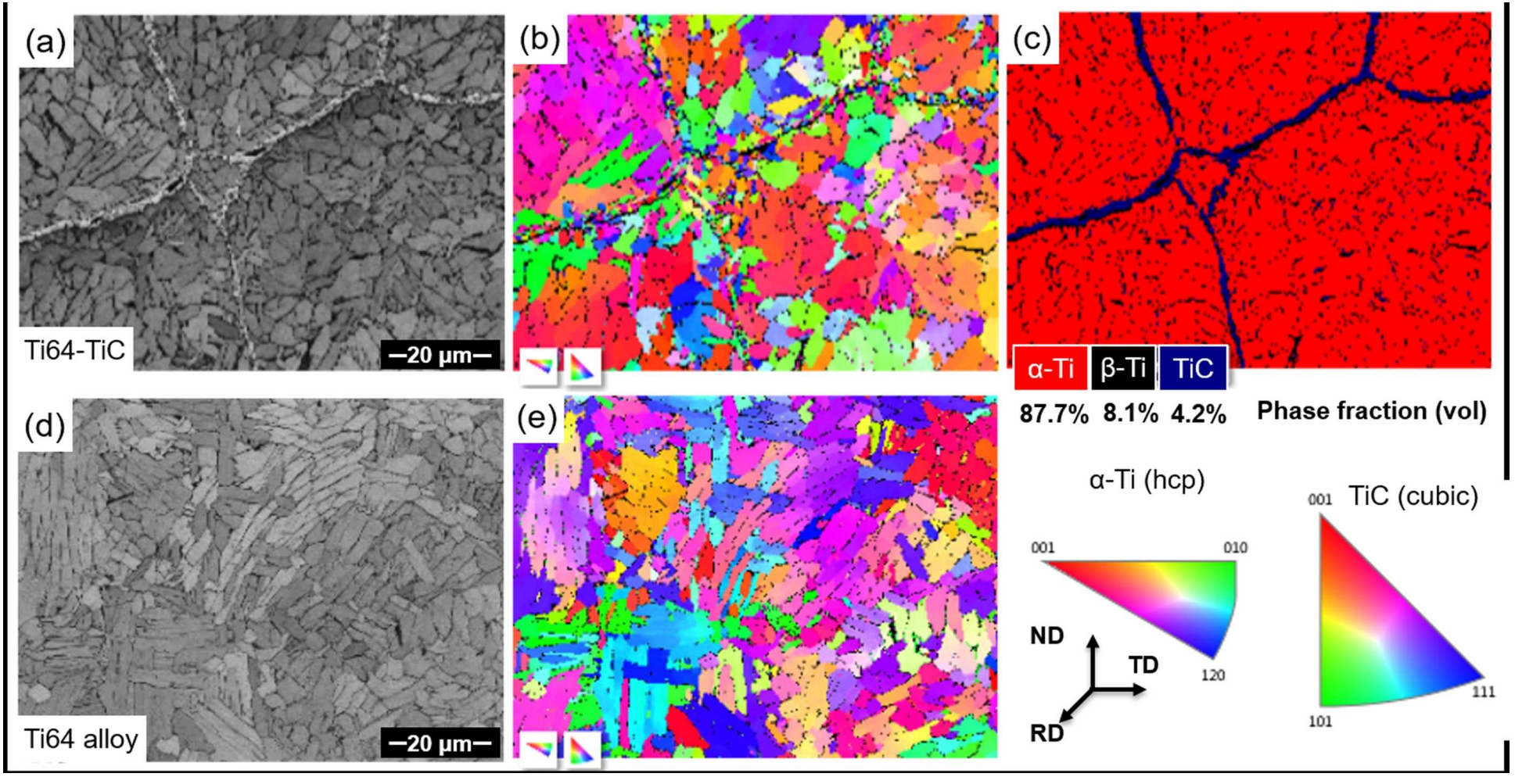
(a)
Ti64-TiC
—20 μm—
(b)
(c)
α-Ti
β-Ti
TiC
87.7%
8.1%
4.2%
Phase fraction (vol)
(d)
Ti64 alloy
—20 μm—
(e)
α-Ti (hcp)
001
010
120
ND
TD
RD
TiC (cubic)
001
111
101

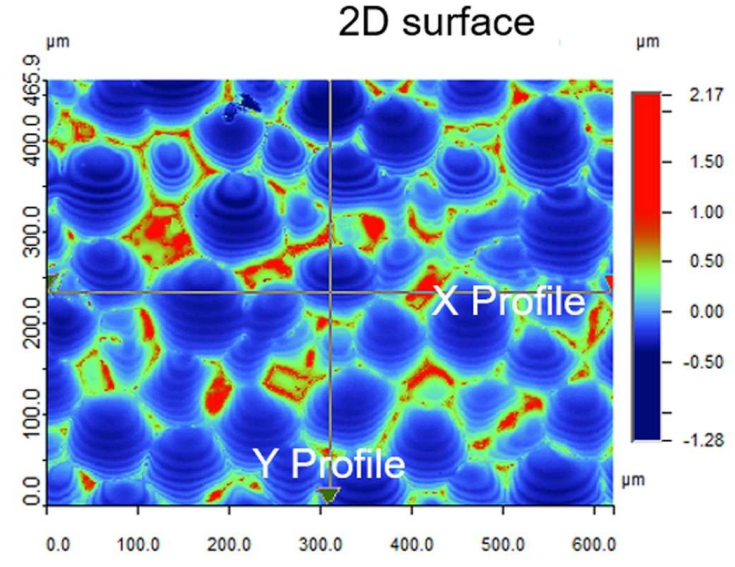
2D surface
µm
465.9
400.0
300.0
200.0
100.0
0.0
X Profile
Y Profile
0.0
100.0
200.0
300.0
400.0
500.0
600.0
µm
2.17
1.50
1.00
0.50
0.00
-0.50
-1.28
µm

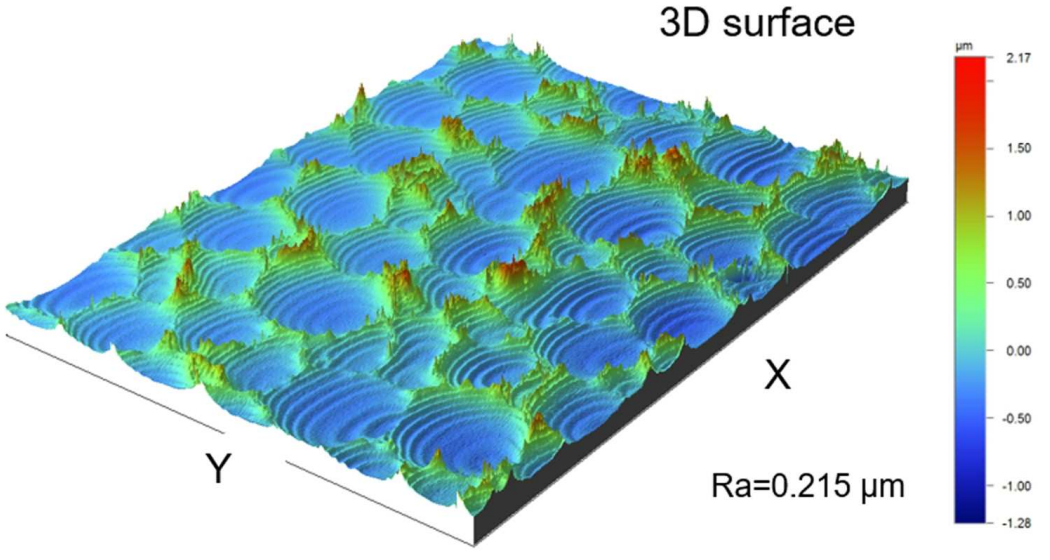
3D surface
X
Y
Ra=0.215 µm
µm
2.17
1.50
1.00
0.50
0.00
-0.50
-1.00
-1.28

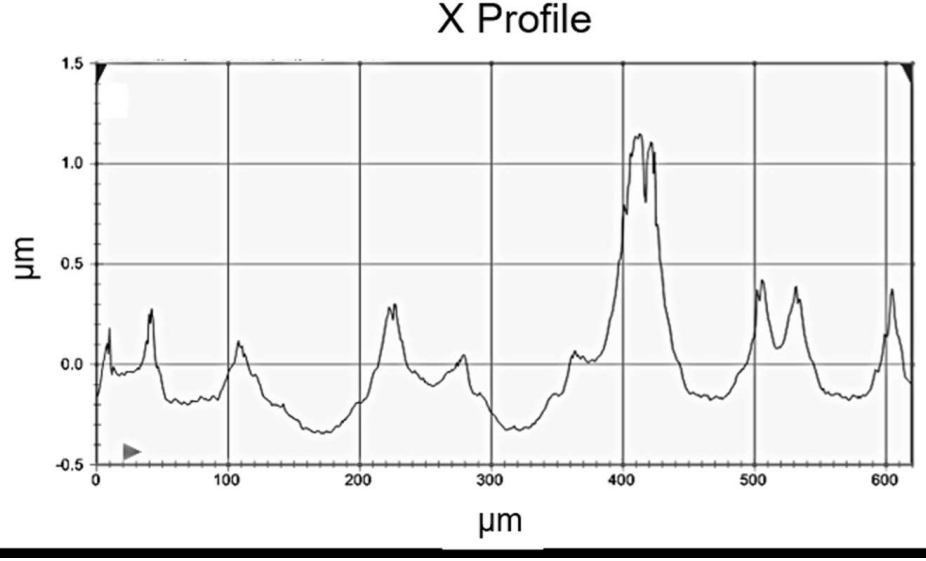
X Profile
µm
1.5
1.0
0.5
0.0
-0.5
0
100
200
300
400
500
600
µm

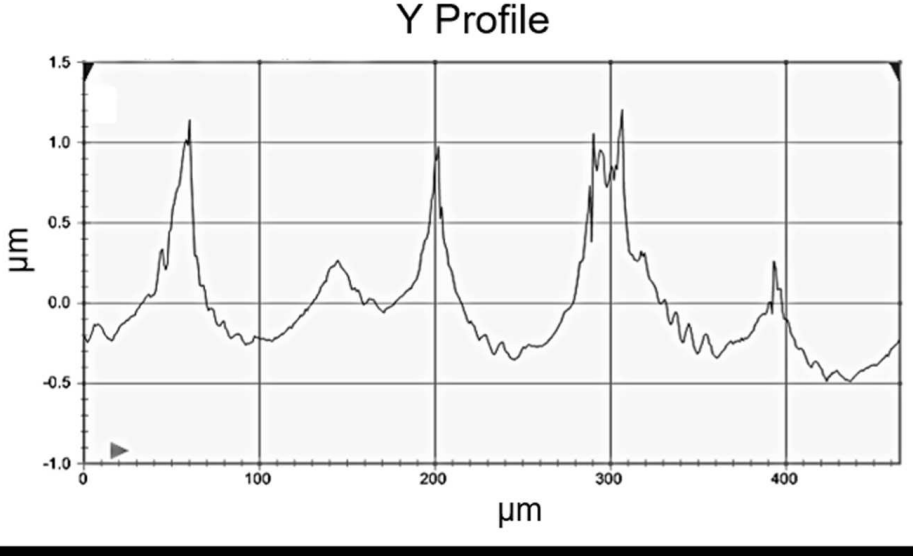
Y Profile
µm
1.5
1.0
0.5
0.0
-0.5
-1.0
0
100
200
300
400
µm

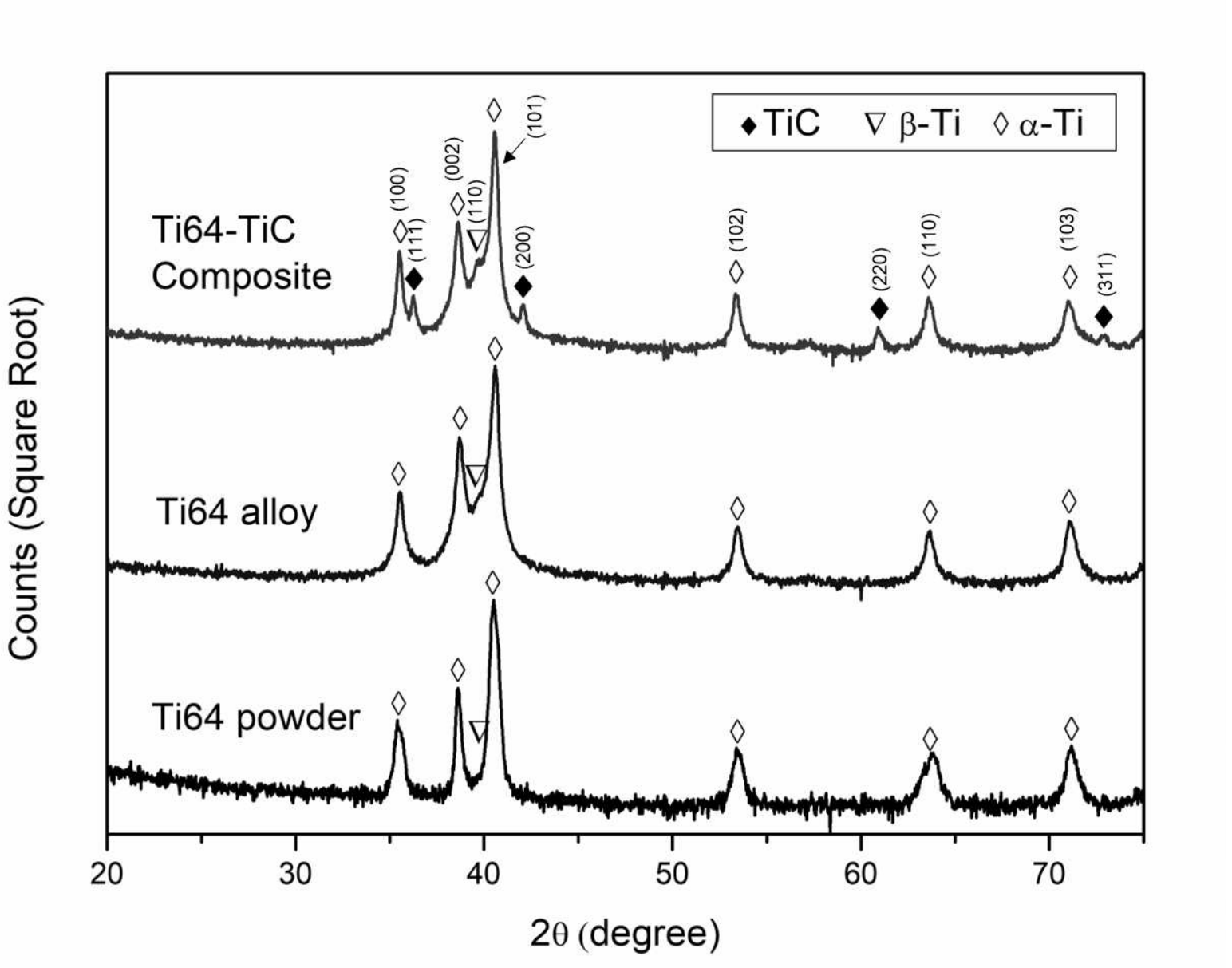
TiC
β-Ti
α-Ti
Ti64-TiC
Composite
Ti64 alloy
Ti64 powder
(100)
(111)
(002)
(110)
(101)
(200)
(102)
(220)
(110)
(103)
(311)
Counts (Square Root)
20
30
40
50
60
70
2θ (degree)

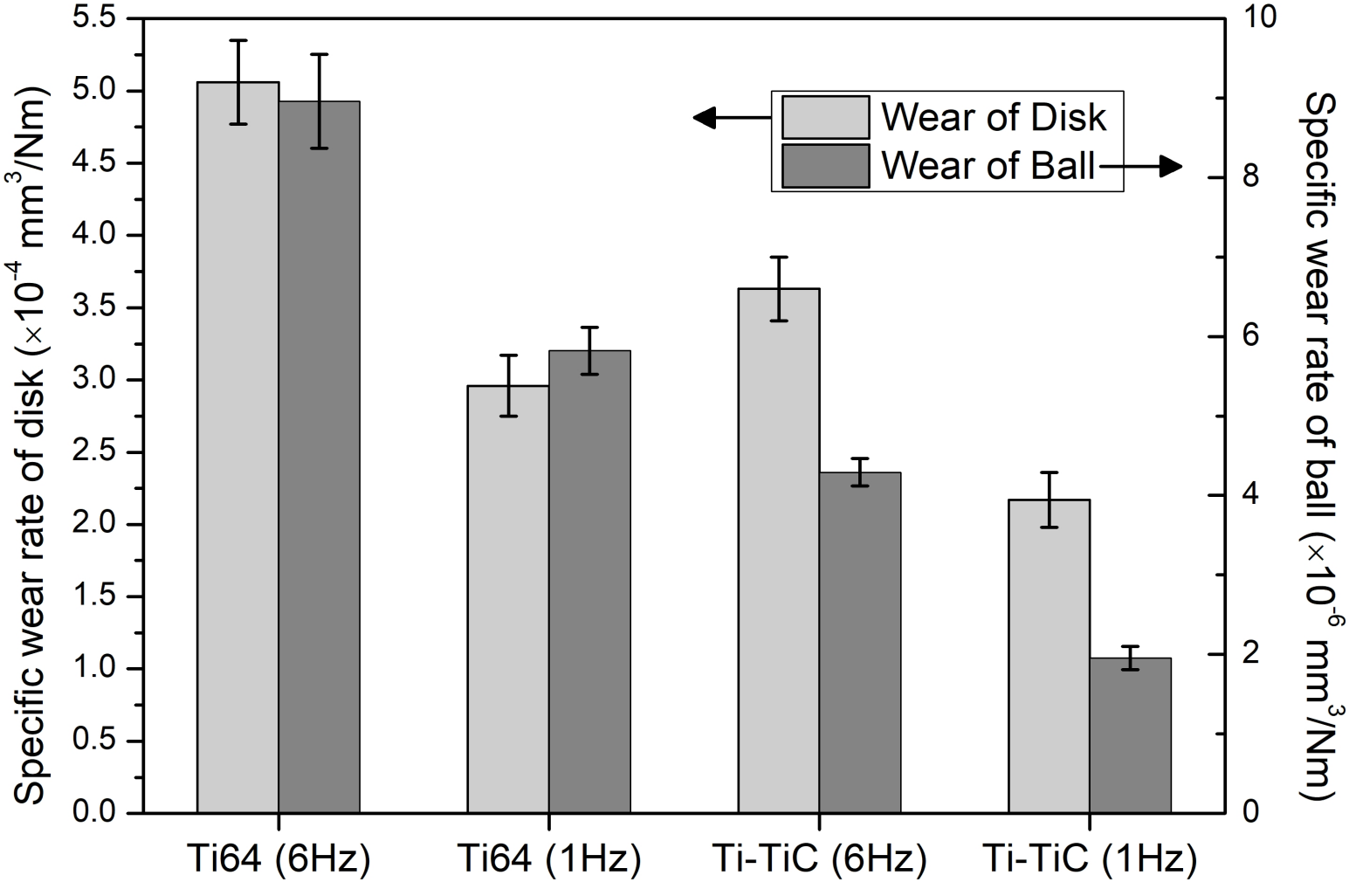
Specific wear rate of disk (×10^-4 mm^3/Nm)
Specific wear rate of ball (×10^-6 mm^3/Nm)
Wear of Disk
Wear of Ball
5.5
5.0
4.5
4.0
3.5
3.0
2.5
2.0
1.5
1.0
0.5
0.0
10
8
6
4
2
0
Ti64 (6Hz)
Ti64 (1Hz)
Ti-TiC (6Hz)
Ti-TiC (1Hz)

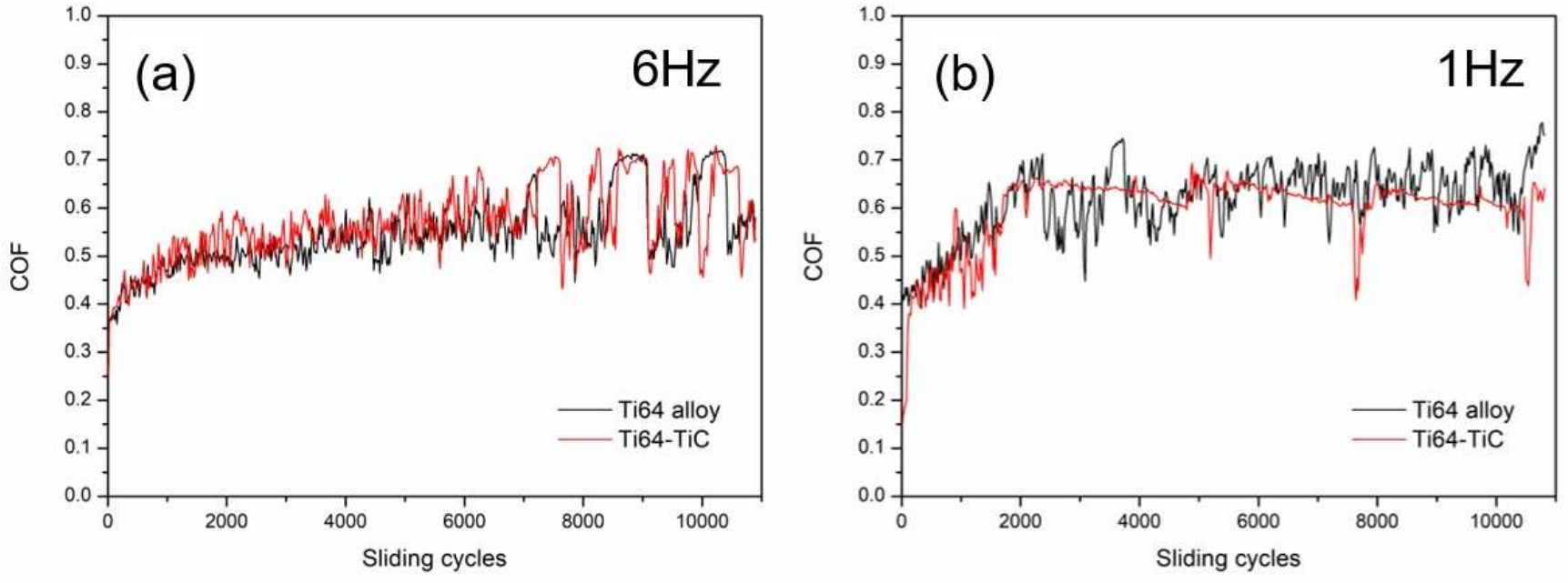
(a)
6Hz
COF
Sliding cycles
Ti64 alloy
Ti64-TiC
(b)
1Hz
COF
Sliding cycles
Ti64 alloy
Ti64-TiC

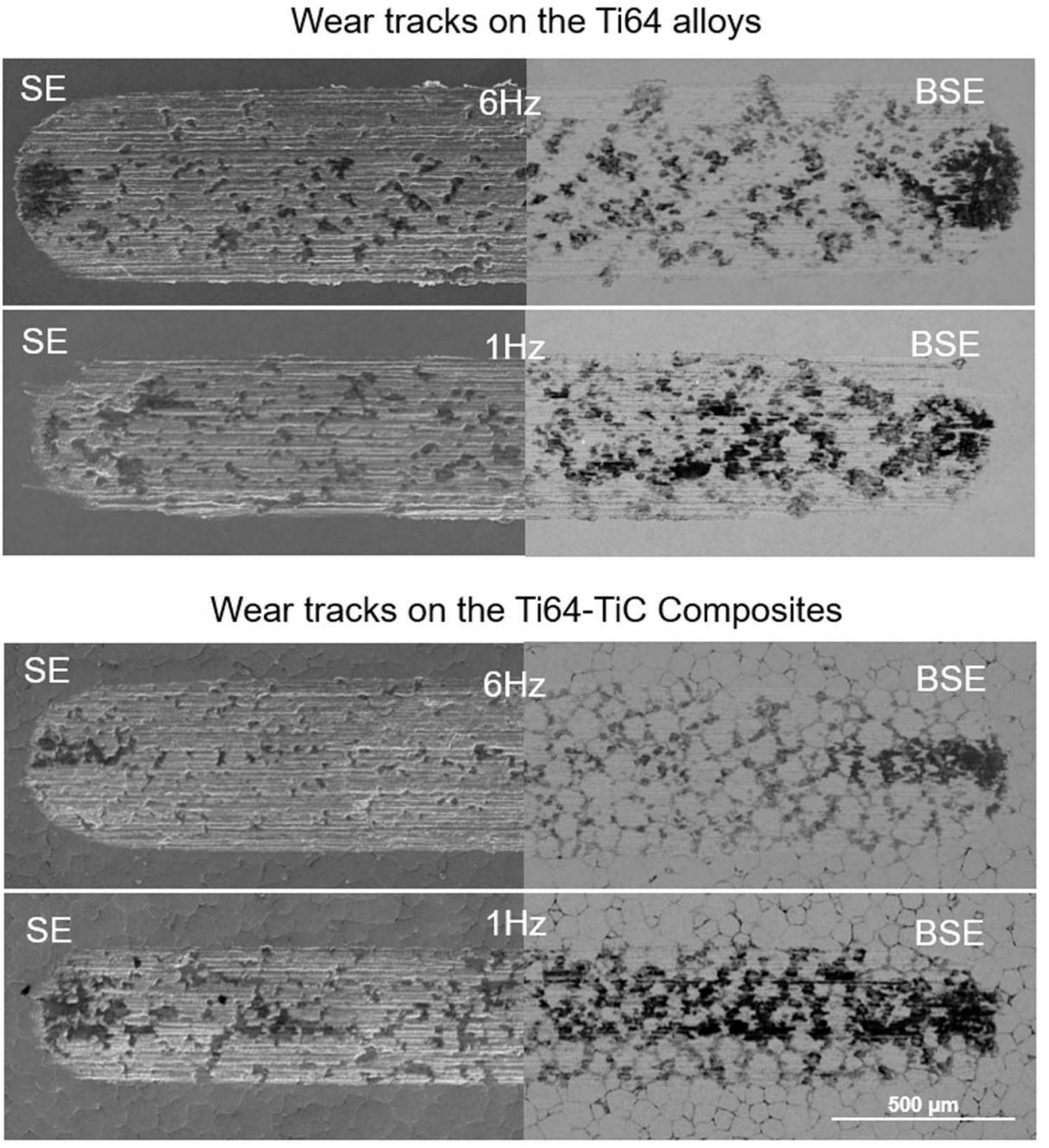
Wear tracks on the Ti64 alloys
SE
6Hz
BSE
SE
1Hz
BSE
Wear tracks on the Ti64-TiC Composites
SE
6Hz
BSE
SE
1Hz
BSE
500 μm

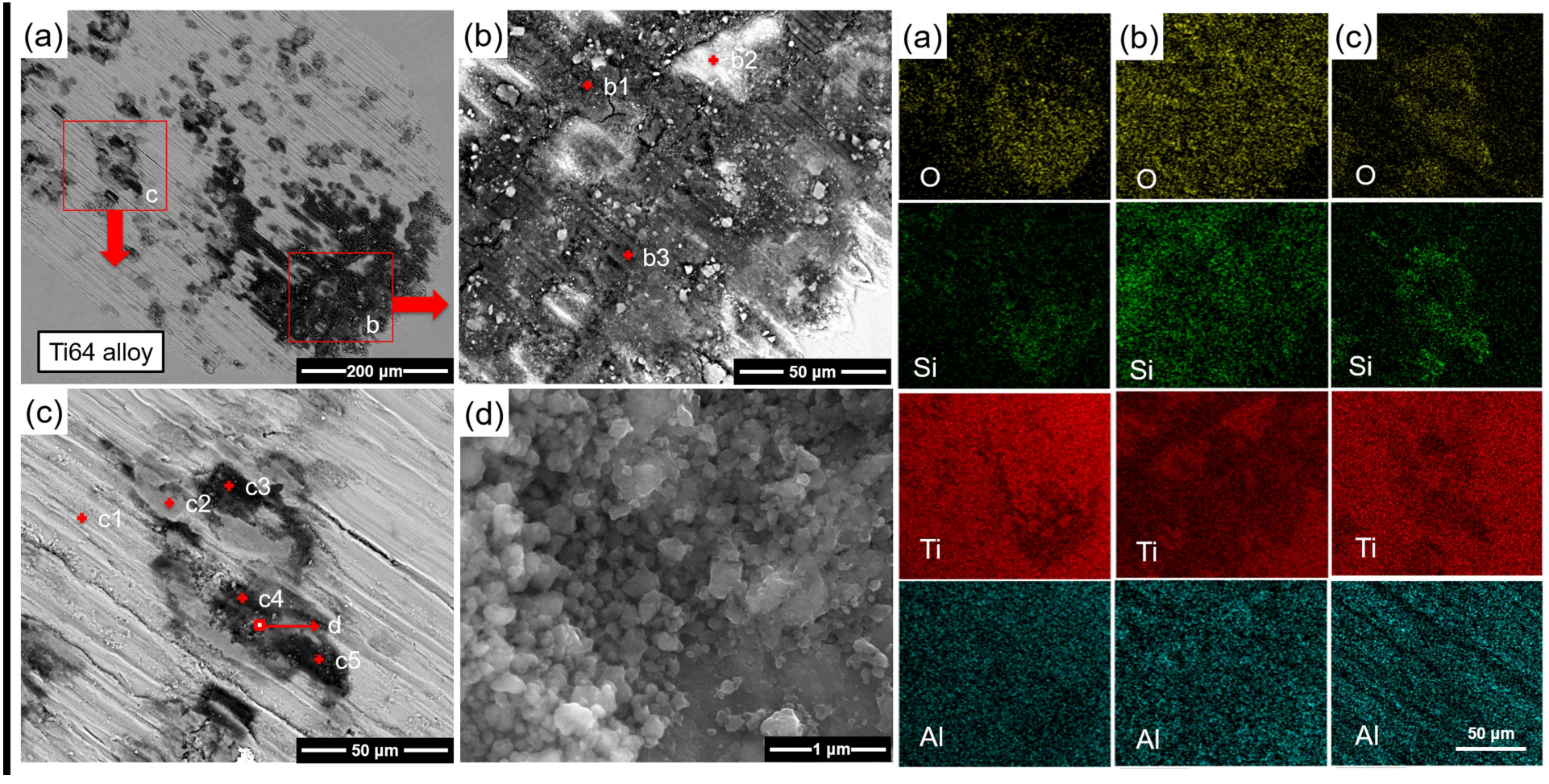
(a)
c
b
Ti64 alloy
200 μm
(b)
b1
b2
b3
50 μm
(c)
c1
c2
c3
c4
d
c5
50 μm
(d)
1 μm
(a)
O
Si
Ti
Al
(b)
O
Si
Ti
Al
(c)
O
Si
Ti
Al
50 μm

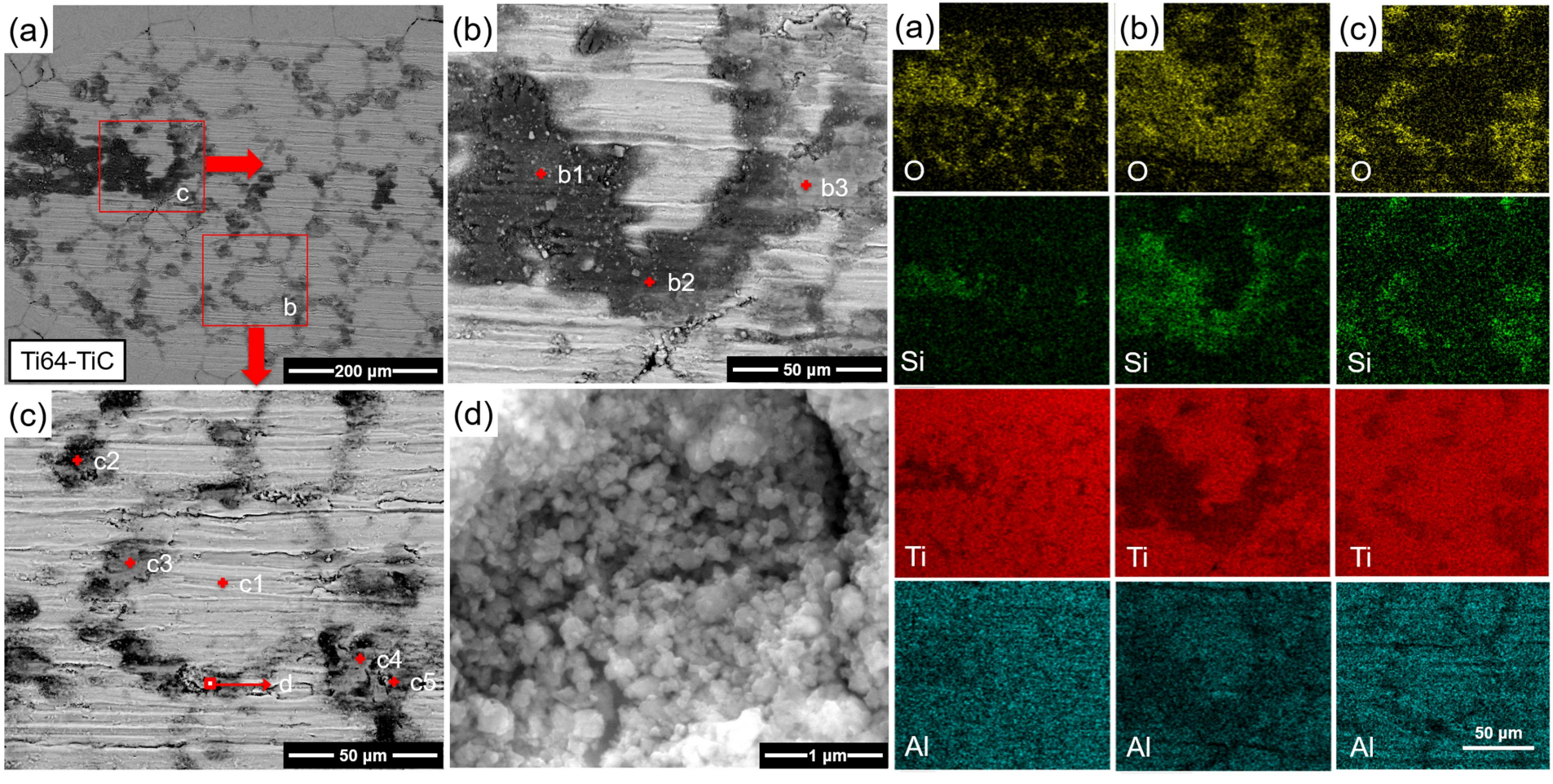
(a)
c
b
Ti64-TiC
200 μm
(b)
b1
b3
b2
50 μm
(c)
c2
c3
c1
c4
c5
d
50 μm
(d)
1 μm
(a)
O
Si
Ti
Al
(b)
O
Si
Ti
Al
(c)
O
Si
Ti
Al
50 μm

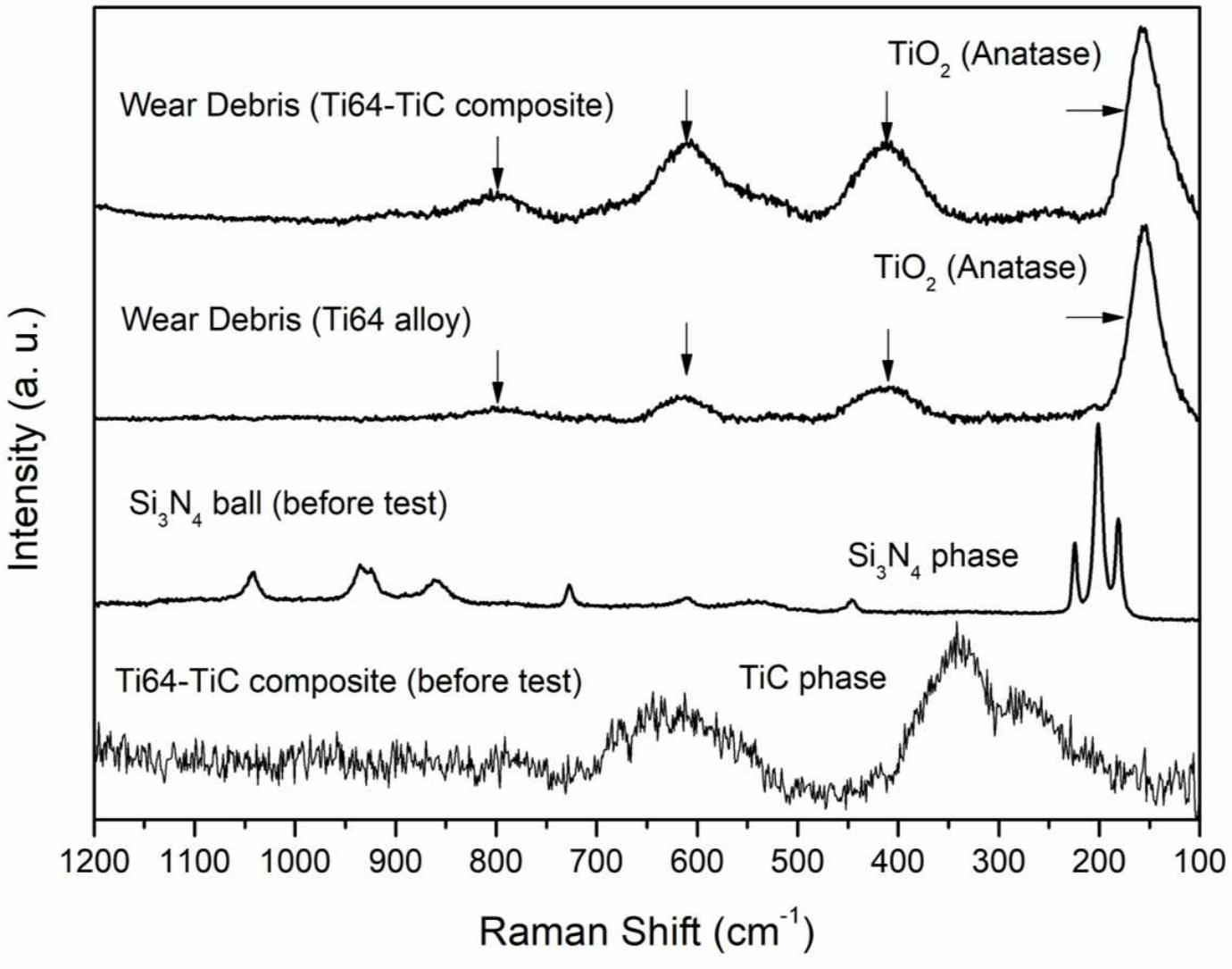
Wear Debris (Ti64-TiC composite)
TiO2 (Anatase)
Wear Debris (Ti64 alloy)
TiO2 (Anatase)
Si3N4 ball (before test)
Si3N4 phase
Ti64-TiC composite (before test)
TiC phase
Intensity (a. u.)
1200
1100
1000
900
800
700
600
500
400
300
200
100
Raman Shift (cm-1)

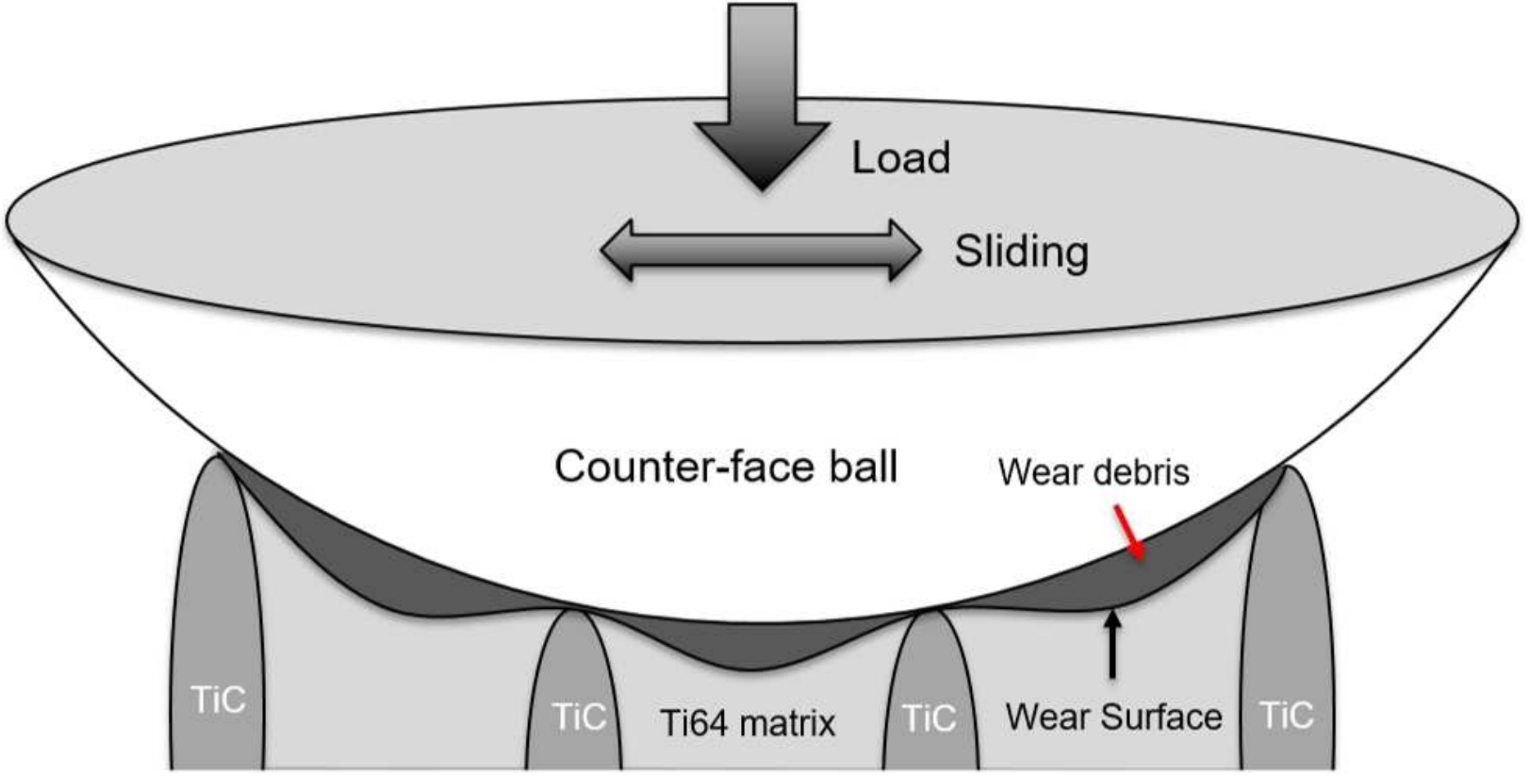
Load
Sliding
Counter-face ball
Wear debris
TiC
TiC
Ti64 matrix
TiC
Wear Surface
TiC

WEAR

Confirmation of Authorship

Please save a copy of this MS Word file, complete and upload as the "Confirmation of Authorship" file.

As corresponding author, I Mingwen Bai, hereby confirm on behalf of all authors that:

1) The authors have obtained the necessary authority for publication.
2) The paper has not been published previously, that it is not under consideration for publication elsewhere, and that if accepted it will not be published elsewhere in the same form, in English or in any other language, without the written consent of the publisher.
3) The paper does not contain material which has been published previously, by the current authors or by others, of which the source is not explicitly cited in the paper.

Upon acceptance of an article by the journal, the author(s) will be asked to transfer the copyright of the article to the publisher. This transfer will ensure the widest possible dissemination of information.